

# Dynamics of Summer Monsoon Current around Sri Lanka

Subham Rath<sup>1</sup>, P. N. Vinaychandran<sup>1</sup>, A. Behara<sup>1</sup>, and C. P. Neema<sup>1</sup>

<sup>1</sup>Centre for Atmospheric and Oceanic Sciences, Indian Institute of Science, Bangalore, India

December 18, 2017

## Abstract

From June–September, the summer monsoon current (SMC) flows eastward south of Sri Lanka and bends northeastward to form a swift jet that enters the Bay of Bengal (BoB). As such, it is a crucial part of the water exchange between the Arabian Sea (AS) and BoB. The processes that determine the evolution, intensification and meandering of the SMC are only partly understood. They involve both local and remote forcing by the wind, as well as interactions with westward-propagating Rossby waves and eddies. In this study, we investigate these processes using an Indian-Ocean general circulation model (MOM4p1) that is capable of simulating the SMC realistically. Because eddies and meanders are smoothed out in the climatology, our analyses focus on a single year of 2009, a period when a strong anticyclonic bend in the SMC was observed.

An eddy-kinetic-energy budget analysis shows the region to be a zone of significant eddy activity, where both barotropic and baroclinic instabilities are active. Based on the analysis, we classify the evolution of SMC into stages of onset, intensification, anticyclonic bend, anticyclonic vortex formation, meandering and termination. In addition, analysis of eddy-potential-vorticity flux and eddy-ensrophy decay reveal when, where, and how the eddies tend to drive the mean flow. Rossby waves and westward-propagating eddies arriving from the east energize the SMC in June and accelerate the mean flow through an up-gradient eddy-potential-vorticity flux. At the same time, local winds also strengthen the flow, by increasing its mean, near-surface, kinetic energy and raising isopycnals, the latter building up available potential energy (APE). The baroclinic instability that takes place in late–July and early–August releases APE, thereby generating the SMC meanders.

arXiv:1711.03311v3 [physics.ao-ph] 15 Dec 2017

# 1 Introduction

The Indian–Ocean (IO) monsoon currents flow south of Sri Lanka, flowing eastward during the summer (named the Summer Monsoon Current; SMC) and westward during the winter (named the Winter Monsoon Current; WMC) [Schott and McCreary, 2001; Shankar et al., 2002]. The SMC plays a particularly important role in the transfer of more saline water from the Arabian Sea (AS) to the Bay of Bengal (BoB) (Murty et al. 1992, Vinayachandran et al. 1999, Jensen 2001).

## 1.1 Background

Figure 1 illustrates the SMC, providing bimonthly plots of the circulation climatology from the Real-time Ocean Surface Current Analysis (OSCAR). The SMC intensifies during May, attains speeds higher than the currents in the other parts of the IO, and makes a northeastward turn into the BoB. There are cyclonic and anticyclonic circulations on the west and east of the strong current, respectively. This pattern remain during July and August, and diminishes in September. It appears every year, albeit with some variation in location and timing.

By compiling data obtained from satellite-tracked drifting buoys, Molinari et al. (1990) first reported eastward flow during the summer near  $10^{\circ}\text{N}$  in the western and central Indian Ocean, naming it the SMC.

Hastenrath and Greischar (1991) described the SMC as being primarily wind driven. The first current-meter measurements in the region revealed the SMC to be shallow (Schott et al., 1994). Using satellite-tracked drifting buoys, Shenoi et al. (1999) reported that the SMC branched around  $87^{\circ}\text{E}$ , with one branch entering the BoB and the other continuing eastward. Expendable bathythermograph (XBT) observations collected between Sri Lanka and the Malaca Strait, together with altimeter data and Oceanic General Circulation Model (OGCM) results, showed the current bends around Sri Lanka and flows into the BoB (Vinayachandran et al., 1999).

Significant eddy activity was also reported in the region during the summer monsoon, based on both drifting-buoy data (Shenoi et al., 1999) and 17 years of altimetry data (Chen et al., 2012). Large barotropic and baroclinic energy conversions are associated with regions of high eddy kinetic energy, suggesting the importance of instabilities in eddy generation (Cheng et al., 2013). Cheng et al. (2013) also commented on the intensification of SMC, suggesting that its probable cause was the conversion of eddy-to-mean kinetic energy during June.

Recently, an international team carried out extensive measurements to investigate monsoon-current dynamics south of Sri Lanka (Lee et al., 2016). Observations from satellite remote sensing, gliders, moorings, drifters, and echo sounders were combined to present a more comprehensive view of the circulation. After crossing the southern tip of Sri Lanka, the SMC flows around the perimeter of a distinct region of shallow thermocline, the Sri Lanka dome (SLD; Vinayachandran and Yamagata, 1998). Lee et al. (2016) also noted strong northward surface geostrophic flow along  $8^{\circ}\text{N}$  between  $83^{\circ}\text{E}$  and  $84^{\circ}\text{E}$ .

A number of modelling studies have investigated SMC dynamics. In companion papers, Shankar et al. (1996) and McCreary et al. (1996) found a southward flow of East Indian Coastal Current (EICC), east of Sri Lanka during the summer, surprising since the current flows *against* the southerly alongshore winds. They determined that the southward flow occurs due to local forcing by a region of strong Ekman suction just east of Sri Lanka.

McCreary et al. (1993) and Vinayachandran and Yamagata (1998) showed that the northward turning is influenced (enhanced) by the arrival of a Rossby wave associated with northward flow from the eastern boundary. Vinayachandran and Yamagata (1998) noted that both Ekman pumping and Rossby-wave arrival determined the life cycle of SLD. A large anticyclonic vortex was found to exist south of Sri Lanka along with an anticyclonic eddy east of SLD; the anticyclonic vortex was formed as a result of barotropic instability. Further, it was found that the arrival of a second Rossby-wave signal (associated with southwestward flow) terminated the northward turning.

Recently, a study by Cheng et al. (2017) on the intraseasonal- to- semiannual variability of sea surface height (SSH) in the southern BoB revealed strong 30-60 day variability east of Sri Lanka. This variability was primarily caused by nonlinear Rossby waves from the east. Further, they showed that the variability at periods greater than 60 days nonlinearly transferred energy to the 30–60-day band.

## 1.2 Present research

In this paper, we continue the effort to understand SMC dynamics. In this study, we seek to understand the processes that are involved in the interaction between the SMC and eddies, and in causing unusually high SMC speed, the meandering of the current, and the ultimate termination of SMC in the southeastern BoB. The relative importance of winds and westward propagating eddies in modulating the mean flow in its various stages is also investigated.

Toward these goals, we analyze a solution to an OGCM which represents the region’s circulation realistically. Eddy-kinetic-energy budget and Transformed Eulerian Mean framework are used to identify regions of eddy-mean flow interaction. To quantify the impacts of local winds, mean wind power integrated over the region of interest is compared with volume integrated mean kinetic energy of SMC above the mixed layer depth. The two quantities are related to each other by the mean kinetic energy equation (section 3). The geostrophic wind power, which is utilised in raising the isopycnals, is also integrated over the study region and compared to the integrated available potential energy (APE).

The mean current circulation in summer (June–September) from during 2004–2009 (Fig. 2) shows the expected north eastward bending of SMC as discussed in Vinayachandran and Yamagata (1998). In addition, the SMC is observed to meander and feed into the southeastern BoB in each of the six years. The climatological map fails to show the meandering of the current. Therefore, we choose a single year of, 2009, for our analyses. This choice is primarily motivated by the study of Vinayachandran et al. (2013), which showed a sharp anticyclonic bend of the current during that year.

### 1.2.1 Key results

Our study divides the evolution of SMC during June–September into six stages—onset, intensification, anticyclonic bending, anticyclonic vortices, meandering and termination. Energy exchanges between background flow and the eddies during these stages are examined. Among these six stages, of particular interest are the stages of intensification, anticyclonic bending, and meandering of SMC. Our work, with the help of energy budget and Transformed Eulerian mean (TEM) approach shows that the effect of eddies in intensifying the SMC is localized to a small region. We found that the strengthening of local winds was primarily responsible for intensification of SMC. The anticyclonic turning of the SMC in early July occurred in response to the local winds as well. Further, the meandering of the SMC was as a result of baroclinic instability (conversion of APE to eddy kinetic energy) which was caused due to fluctuating wind power.

The paper is organized as follows. In Section 2, we provide model overview and compare model output with observations. Section 3 is based on eddy kinetic-energy-budget analysis. In Section 4, we present the evolution of SMC and discusses its five stages with the help of energetics and Transformed Eulerian mean (TEM) approach. Also, investigate the role of the local winds in these stages. In Section 5, a summary of our findings is provided.

## 2 The model

The OGCM used in our study is the Modular Ocean Model (MOM), a numerical ocean model based on hydrostatic primitive equations. The model configuration, forcings as well as boundary conditions used in this study are the same as in Das et al. (2015). So, only a brief overview is given here.

The model domain is the tropical IO, extending from 30°S to 30°N and from 30–120°E. Its horizontal resolution is 0.25° in both latitude and longitude. It has variable resolutions in the vertical with 58 levels, 44 of which are in the top 200 m, and 1-m resolution is used in the top 18 m. Bottom topography is based on modified ETOPO5 bathymetry (Sindhu et al., 2007). Continental boundaries within the domain are treated as solid walls, and sponge layers are applied long the southern model boundary and along portions of the eastern boundary (Kurian and Vinayachandran, 2007). Vertical mixing is the K-profile parametrization (KPP) scheme (Large et al., 1994), and horizontal mixing scheme follows Chassignet and Garraffo (2001). Vertical diffusivity and viscosity are based on dissipation mechanisms associated with internal wave breaking (Simmons et al., 2004) and bottom drag experienced by barotropic tides (Lee et al., 2006), respectively. The model equation of state is the same as that in Jackett et al. (2006). The model is spun up for 10 years using climatological forcing, which is then switched to daily varying interannual forcing (see Vinayachandran et al. (2012) for details).

Figure 3 compares observed and modelled, surface currents during June, July, and August of 2009. Large-scale features of the circulation are well simulated, except that the model underestimates the current speed. Small scale features, such as anticyclonic eddies during

July and August, were more prominent in the observations. For example, during July and August the OSCAR product show a continuous meandering of SMC, whereas an anticyclonic vortex is found together with the SMC as it entered the BoB in the model. During August, two vortices were present to the right of the SMC in the model. The northern vortex in the model did not exist in the observation.

### 3 Eddy activity

#### 3.1 Mean and eddy kinetic energy

To investigate the eddy-mean flow interactions that impacts the SMC, we divide all the field variables of interest into a background (mean) and eddy component. In our study, we have taken 120 day low-pass filtered state as the mean component and 120 day high-pass filtered state as the eddy component (see Appendix A). The kinetic energy is also split into mean kinetic energy (MKE) and eddy kinetic energy (EKE). Following (Masina et al., 1999) notation, MKE is defined by

$$K = \rho_0 \frac{\bar{u}_i^2}{2} \equiv \rho_0 \left( \frac{\bar{u}^2 + \bar{v}^2}{2} \right), \quad (1)$$

and determined by the prognostic equation

$$\underbrace{\frac{\partial}{\partial t} K}_A + \underbrace{\rho_0 u_j \frac{\partial}{\partial x_j} \frac{\bar{u}_i^2}{2}}_B = - \underbrace{\frac{\partial}{\partial x_i} \overline{P u_i}}_C - \underbrace{\rho_0 \bar{u}_i \frac{\partial \overline{u'_i u'_j}}{\partial x_j}}_D - \underbrace{g \bar{\rho} \bar{w}}_E + \underbrace{\bar{u}_i \cdot \bar{D}}_F + \underbrace{\bar{u}_i \cdot \bar{F}}_G. \quad (2)$$

A : MKE tendency

B : Advection of MKE

C : Pressure divergence flux

D : Eddy momentum flux convergence

E : Conversion mean potential energy (MPE) to MKE

F : Dissipation

G : MKE change due to external forcing

Similarly, EKE is defined by

$$K' = \rho_0 \frac{u_i'^2}{2} \equiv \rho_0 \left( \frac{u'^2 + v'^2}{2} \right), \quad (3)$$

and determined by the prognostic equation

$$\underbrace{\frac{\partial}{\partial t} K'}_{A'} + \underbrace{\rho_0 (\bar{u}_j + u'_j) \frac{\partial}{\partial x_j} \frac{u_i'^2}{2}}_{B'} = - \underbrace{\frac{\partial}{\partial x_i} (P' u'_i)}_{C'} - \underbrace{\rho_0 u'_i u'_j \frac{\partial \bar{u}_i}{\partial x_j}}_{D'} - \underbrace{g \rho' w'}_{E'} + \underbrace{u'_i \cdot \mathcal{D}'}_{F'} + \underbrace{u'_i \cdot \mathcal{F}'}_{G'}. \quad (4)$$

$A'$  : EKE tendency

$B'$  : Advection of EKE

$C'$  : Eddy pressure divergence flux

$D'$  : Deformation work due to mean flow

$E'$  : Baroclinic energy conversion

$F'$  : Eddy dissipation

$G'$  : EKE change due to external forcing

### 3.1.1 EKE structure

Figures 4a and 4b show the time mean (June–September) vertically integrated (top 100 m) map of EKE and depth-longitude section at 6.5°N, respectively. The magnitude of EKE is consistent with the findings of Chen et al. (2012). Maximum EKE appeared between 83–85°E in the form of two distinct high-value cores extending to 120 m. Figures 4c and 4d show the surface-layer averaged (top 30 m) time mean velocity maps and depth-longitude section of velocities at 6.5°N, respectively. High speeds of SMC existed between 83–85°E and extended up to a depth of 120 m, consistent with the shallow nature of SMC in the observation.

### 3.1.2 Time series

Figure 5 shows the time series of volume-integrated MKE and EKE between 82–86°E, 5–8°N in the top 100 m. The MKE is about four times larger in magnitude than the EKE (Fig. 5a). This difference shows eddies only had a secondary contribution in driving the mean flow, which implies that the mean flow was largely wind driven when integrated over a large domain. However, the effect of eddies in driving the mean flow became more significant when integrated over a smaller domain (84–85°E and 5–7°N) as the peak MKE was twice the peak EKE now (Fig. 5b). Thus, fractional transfer from EKE to MKE is unlikely to bring in significant changes in SMC speed throughout the domain, but the effects at smaller scales are prominent as will be discussed later (Section 4.2.1).

## 3.2 Instabilities

Instabilities are associated with energy conversions. Barotropic instability converts MKE to EKE, and is represented by term  $D'$  in (4), which when expanded has the form

$$-\rho_0 u'_i u'_j \frac{\partial \bar{u}_i}{\partial x_j} = -\rho_0 \left( u'v' \frac{\partial \bar{u}}{\partial y} + v'v' \frac{\partial \bar{v}}{\partial y} + u'u' \frac{\partial \bar{u}}{\partial x} + u'v' \frac{\partial \bar{v}}{\partial x} \right). \quad (5)$$

Since the terms in (5) are of the same magnitude all are retained in our analyses. Baroclinic instability converts APE into EKE. It is represented by the term  $E'$  ( $-g\rho'w'$ ) in (4). For both instabilities, positive value of each terms implies energy conversion from the background state to eddies.

### 3.2.1 Horizontal and vertical structures

Figures 6a and, 6c show time mean vertically integrated (top 100 m) maps of barotropic and baroclinic energy conversions, respectively. Figures 6b and 6d are the respective depth-longitude sections of the energy conversions at 6.5°N. Barotropic energy involving both mean-eddy and eddy-mean energy conversions between (83°E–85°E) and (5°N–7°N). Eddies are found to extract energy out of the mean flow west of 84°E through barotropic instability and transfer energy to the mean flow east of 84°E. Significant baroclinic energy conversion was also found (Figs. 6c, 6d), indicating that the SMC is characterized by mixed instabilities. Depth–longitude section along 6.5°N reveals barotropic energy conversion from mean to eddies, extending to 100 m, while the baroclinic energy conversion was maximum between 60 and 80 m centered around 84°E.

## 3.3 Intraseasonal Rossby waves and eddies

Figure. 7 (top panel) is a Hovmöller diagram of high-pass-filtered meridional velocity. Westward-propagating signals with speeds of about 15.5 cm/s started at 90°E and propagated across the basin. In particular, a signal associated with northward flow was at 90°E in May and reached 84°E by mid-June. It was followed by a signal with southward flow that arrived near 84°E about mid-July. Note that the propagation speed of the latter signal decelerated toward the west (the band tilted more sharply), likely due to interaction with the SMC.

Dispersion diagram from high-pass-filtered meridional velocity component (Fig. 7) shows a probable Rossby wave structure with a 40–50 day signal corresponding closely to baroclinic mode 2. The south and east of Sri Lanka was characterized by the interactions of Rossby waves and other probable eddies with the SMC and is consistent with the findings of Vinayachandran and Yamagata (1998). Rossby wave phase speed calculated from the dispersion diagram was approximately 17 cm/s, consistent with the Hovmöller diagram.

## 4 Evolution of SMC

The background flow (120-day low-pass component in our case) varied greatly during the summer monsoon. Thus, the processes that were significant at different phases of SMC as it evolved are presented in this section. Evolution of SMC is shown along with the dominant processes involved, for selected days of the 2009 summer monsoon in Figs.8–14. Five-day running average was applied to all the quantities to smoothen out rapid fluctuations. Evolution of SMC and the processes associated with upper-layer currents, their high-pass and low-pass components and analysis of energetics are shown. The low-pass current had a zonal orientation east of Sri Lanka at the onset of summer monsoon in late–May. It gradually developed a northeastward turn in mid–June, and was associated with an anticyclonic vortex in July. The current gradually meandered in August and fed into the southeastern BoB. The evolution of SMC viewed from energetics perspective unfolds some important features.

### 4.1 Onset

Onset of summer monsoon in 2009 was in late–May (Das et al., 2015). With the onset, the wind became south-westerly and gained strength. Circulation around Sri Lanka during this time comprised of three different current systems: (1) a zonal flow east of Sri Lanka, (2) a southeastward current south of Sri Lanka, and (3) a downwelling eddy (positive sea level anomalies) centered around  $87^{\circ}\text{E}$ ,  $3^{\circ}\text{N}$  (Fig. 8a). With the advent of westward propagating eddy, the southeastward current merged with the zonal current around  $5^{\circ}\text{N}$ . The current was blocked by the eddy and it fed into the zonal flow east of Sri Lanka. As the anticyclonic eddy was associated with prominent EKE, density surfaces along  $85^{\circ}\text{E}$  developed a poleward slope with a sharp gradient between  $5^{\circ}\text{N}$  and  $7^{\circ}\text{N}$  (Fig. 8b). The MKE around this time started increasing (Fig. 8c). However, no notable barotropic or baroclinic energy conversions took place during this time (Fig. 8d, 8f).

### 4.2 Intensification

As the eddy moved further westward, the circulation system east of Sri Lanka was characterized by negative barotropic energy conversion (Fig. 9d). This implies wave–induced accelerations to the developing SMC, that was reflected by the intensification of surface current, was restricted to a particular region (Figs. 9a, 10a). The current intensified further in June with little mean to eddy energy conversion noticed along  $83^{\circ}\text{E}$ , as the southward flowing current along the east coast of Sri Lanka merged with the north-eastward SMC. The 120-day high-pass filtered eddy pushed the mean flow northward. The eddies thus seemed to impose an acceleration tendency on the SMC (Fig. 10a).

To understand when these eddies caused the SMC to intensify, we use the TEM approach to modify the momentum and density equations. The advantage of using TEM approach is that it allows the eddy forcing to appear only in the horizontal momentum equation. We also



use the quasi-geostrophic (QG) approximation, so that the only eddy forcing in the TEM equation is reduced to eddy potential vorticity (PV) flux (see Appendix B). Insights from eddy enstrophy equation helps identify where the eddies tend to drive the mean flow.

#### 4.2.1 Where did eddies cause this intensification?

Whether the eddies tend to drive the mean flows or lead to loss of momentum in the mean flow depends on the nature of PV fluxes relative to the mean PV gradient. For eddies to drive mean flow, eddy PV flux has to be upwards relative to the mean potential vorticity gradient (Holland and Rhines, 1980), hence also known as upgradient eddy PV flux. This can be understood in terms of the general enstrophy equation (Wilson and Williams, 2004),

$$\frac{\partial q'^2}{\partial t} + \nabla \cdot \mathbf{u} \frac{q'^2}{2} + \mathbf{u}'q' \cdot \nabla \bar{q} = -D \quad (6)$$

where  $\bar{q}$  is the mean PV,  $q'$  is the eddy PV and  $D$  represents the dissipation of eddy enstrophy, all other symbols bearing their usual meanings as discussed earlier. A positive dissipation would lead to eddy enstrophy decay. First term on the left hand side of the equation (6) represents the local rate of change of eddy enstrophy, second term gives the divergence of eddy enstrophy advection and third term however gives us the eddy enstrophy decay termed here as *eddy destruction*.  $\nabla \cdot \mathbf{u} (q'^2/2)$  is termed as “enstrophy destruction” term as the latter dissipates the eddies by fluxing PV into the mean flow. Negative of  $\nabla \cdot \mathbf{u} (q'^2/2)$  can be thought of as generation of eddies as it leads to local increment in eddy enstrophy in (6). For the eddies to drive mean flow there has to be a decay of eddy enstrophy in the vicinity of eddy mean flow interaction. The second term can be considered as a higher order term in the equation which helps us to identify regions of convergence and divergence of eddy enstrophy flux.

Insights from the eddy destruction (Fig. 15b) help to identify regions of upgradient eddy PV flux. Here the eddies try to drive the mean flow by accelerating the latter. Regions of high velocities in the SMC are found to be associated with upgradient eddy PV flux. Upstream the eddy PV flux is downgradient indicating regions where eddies extract momentum and energy from mean flow. The region is also characterised by positive eddy PV flux downstream and negative upstream (Fig. 15c). This implies that the eddies extract momentum and energy from the SMC upstream. The same region is also barotropically unstable as found from energy considerations (Fig. 6).

#### 4.2.2 When did eddies cause this intensification?

Time series of eddy PV flux,  $v'q'$  provides a more comprehensive view of the eddy mean flow interaction. Regions where the eddies tended to drive SMC are identified (Fig. 15b) and a location has been chosen from the region to identify when the eddies caused an acceleration tendency on the mean flow. The time series of eddy PV flux at 84°E, 6.5°N and at 50–m depth indicates a sharp positive peak in mid–June (Fig. 15d). This coincided with the arrival of the Rossby waves and westward propagating eddies in the region. Thus, the

eddies, because of positive values of  $v'q'$  (see Appendix B, C) could be expected to provide an acceleration tendency to the mean flow as they arrived and interacted with the latter in mid-June. Throughout July, the eddy PV flux remained relatively low at the location. Positive eddy PV flux was observed in late-August and early-September, but by this time, the SMC already started to weaken and disappear.

### 4.2.3 Local winds

However, the local winds also became very strong over the region during this time, and thus could influence the MKE significantly (Fig. 9c). The MKE of the ocean current is related to the mean wind power in equation (2) as

$$\int_V \rho_0 \frac{\partial \overline{\mathbf{u}^2}}{\partial t} dV \sim \int_A \overline{\mathcal{F} \cdot \mathbf{u}} dA = \int_A \overline{\boldsymbol{\tau} \cdot \mathbf{u}} dA \quad (7)$$

where  $\tau$  is the wind stress. Figures 18a and 18b shows the variation of mean wind power input along with MKE, integrated over the top 40 m within the surface mixed layer. Both quantities are integrated over 82–86°E, 5–8° N. The MKE increased with the increase in total mean wind power in June, peaked in late-June following the variation of mean wind power, and started to decline from mid- July. Thus, the wind can be considered as the predominant driving agent in intensifying mean SMC flow.

## 4.3 Anticyclonic bend

At the beginning of July, part of the SMC started to take an anticyclonic turn near 85°E, while the other part continued to flow northeastward (Fig. 11a, 11c). The MKE was high in the region during this time (Fig. 11c), while the EKE was significantly low (Fig. 11e). Barotropic energy conversion was also very small (Fig.11d). However, some baroclinic energy conversions took place north of the SMC, where it took cyclonic turn (Fig. 11f). Density surfaces within 40–100 m along 85°E were suppressed between 5°N and 7°N, with a poleward gradient, which resulted in the generation of APE. In mid-July, the anticyclonic turn of the SMC became more prominent associated with high MKE but low EKE. Barotropic energy conversion was very low in the region, while positive baroclinic energy conversion existed along the SMC. Negative baroclinic energy conversion implying an increase in eddy available potential energy can be found on both sides of the SMC. But, this does not adequately explain the bending of the SMC. The anticyclonic turning of the low-pass current could also be due to the local winds in the region. The ageostrophic component of the current supported this possibility (Fig. 16). The ageostrophic currents were larger and modulated the background flow in the absence of prominent eddies in the region during the time. The baroclinic energy conversion observed could be due to the variation in wind energy input, leading to the fluctuation of the density surfaces (to be discussed next).

## 4.4 Anticyclonic vortices

In late–July (Fig. 12a), an anticyclonic vortex was fully developed and centered around 84°E. In addition to the anticyclonic turning of the low-pass background current, an anticyclonic eddy associated with strong EKE appeared in this region. Both barotropic and baroclinic energy conversions were responsible for the generation of these eddies.. The SMC at 83°E, 6°N became barotropically unstable, leading to the conversion MKE to EKE (Fig. 12d). Baroclinic instability also appeared around 7°N associated with flattened isopycnals that weakened the flow and could cause the current to meander (Fig. 12f). Significant baroclinic energy conversion appeared all along the outer periphery of the anticyclonic vortex. In mid–July, at around 89°E, 8°N, the SMC encountered another anticyclonic eddy, which remained non-interacting in terms of energy exchanges. Later in late–July, due to the gradual meandering pattern of the current, the eddy around 8°N further intruded into the SMC (Fig. 12a). This eddy was termed as an Intermediate Geostrophic (IG) eddy (Vinayachandran and Yamagata, 1998).

## 4.5 Meandering

Horizontal shear of the SMC was reduced as a result of barotropic instability. Further, in early–August (Fig. 13b), the sloping density surfaces flattened, releasing a large amount of APE. Baroclinic instability associated with this flattened density gradients and meridional buoyancy flux was the dominant mechanism leading to the growth of disturbances (Fig. 13f). The combined effect of barotropic and baroclinic instabilities weakened the SMC which now meandered because of baroclinic instability (Ikeda, 1981). One possible reason behind the release of APE in late–July and August could be the gradual weakening of local wind power.

### 4.5.1 Local wind power

The wind power is calculated by

$$W = \iint_A \boldsymbol{\tau} \cdot \mathbf{u} dA, = \iint_A (\boldsymbol{\tau} \cdot \mathbf{u}_g + \boldsymbol{\tau} \cdot \mathbf{u}_{ag}) dA,$$

where  $\boldsymbol{\tau} \cdot \mathbf{u}_g$  is the geostrophic wind power while  $\boldsymbol{\tau} \cdot \mathbf{u}_{ag}$  is the ageostrophic wind power. The geostrophic wind work is utilized in vertically displacing the isopycnals thereby influencing APE (Brown and Fedorov, 2010) via Ekman pumping, upwelling and downwelling. On the other hand, the ageostrophic wind work is required to maintain the Ekman spiral (Huang, 2010).

Figure 17 shows time-mean (June–September) maps of total wind power (combining geostrophic and ageostrophic), baroclinic energy conversions, MKE and EKE, vertically integrated over 100m depth. The wind power, MKE and EKE together with baroclinic energy conversions are also found to be significantly high over this region.

### 4.5.2 Available potential energy

APE can be defined as difference between total potential energy and minimum total potential energy which could result from any adiabatic redistribution of mass. It can be regarded as a deviation from the resting (minimum energy configuration) stable stratification state. To estimate local APE, we calculate it in Joules as Oort et al. (1989)

$$E_p = -\frac{g}{2} \iiint_V \frac{(\rho - \bar{\rho})^2}{\partial \bar{\rho} / \delta z} dV. \quad (8)$$

APE has been integrated over 82–86°E, 5–8°N and from the surface to 100 m.

Figures 18c and 18d shows the relationship between wind power and volume integrated APE. The APE corresponded well with the variation in wind power. Only in the month of June, the APE remained unchanged for some time inspite of increasing wind power. The arrival of downwelling Rossby waves associated with suppressed thermocline could negate the influence of wind power. In late-June, APE again started to respond to change in wind power. During this time, the local wind power probably overwhelmed the effects of westward propagating eddies. Significant amount of APE reduction started from mid-July and continued till August, which was associated with the possibility of major baroclinic instability taking place at the depth.

### 4.5.3 Westward propagating eddies

Before this stage, the westward propagating eddy at 8°N that did not interact with the SMC (Figs. 12d, 12f), started exchanging energy with meandering current (Figs. 13d, 13f). One possible reason could be the weakening of the SMC as a result of baroclinic instability, which now reached the critical level (a level where exchange of energy takes place between mean flow and wave). The interaction of this eddy with the SMC lead to barotropic energy conversions at 85°E, 6° N (Fig. 13d). This rendered the current barotropically unstable and merely amplified the recirculation at 8°N, and the current was thus found to meander and feed into the southeastern BoB (Fig. 13a).

## 4.6 Termination

In late August and September, the continuous SMC disappeared (Fig. 14a). The anticyclonic eddy near 8°N pushed against the weakened SMC and moved it westward. The entire meandering pattern shifted slightly to the west and by mid-September (Fig. 14a) the SMC system disappeared.

## 5 Summary and conclusions

The SMC around Sri Lanka plays a crucial role in the interaction of the water masses between the two basins on either side of India, namely, the Arabian Sea and Bay of Bengal. Past studies showed that the SMC is highly energetic and eddy activity is intense in this region (Vinayachandran and Yamagata, 1998, Shenoi et al., 1999, Chen et al., 2012). The prime objective of our analysis was to understand the evolution, including the intensification and meandering of the SMC, using an OGCM (MOM4p1). We made several new contributions toward understanding the evolution of SMC around Sri Lanka, which involve eddy–mean flow interactions and effect of local versus remote forcing on the dynamics in the region. Analysis of eddy potential vorticity eddy potential vorticity flux, eddy entrophy, eddy energy budgets were carried out which shed new insights on how the eddies drove the mean flow and vice versa. The study also provided better understanding of the influence of stratification in terms of driving the mean flow and isolating the role of winds in affecting the circulation. The evolution of SMC was classified into six stages, namely, onset, intensification, anticyclonic bend, anticyclonic vortices, meandering, and termination. Barotropic and baroclinic energy conversions were the dominant mechanisms to modulate the background flow of the SMC.

The arrival of Rossby waves and westward propagating eddies into this region resulted in high eddy momentum flux exchange in the month of June. Using the TEM approach and combining the net effect of momentum and buoyancy fluxes, we showed that the eddies imparted PV flux and induced acceleration tendency on the mean flow in mid–June. Using quasi-geostrophic approximation to understand the effect of eddies on the mean flow, we found that there were regions of up-gradient eddy PV flux where the eddies drove the mean flow. There were also upstream regions associated with down-gradient eddy PV flux where the eddies extracted energy and momentum out of the mean flow. Local winds affected both the mean flow of the SMC and its course path during the summer monsoon. The volume-integrated MKE was at least twice that of EKE, suggesting that the circulation in this region was largely wind driven. Also, the time-mean (June–September) maps of mean kinetic MKE corresponded well with the wind power. The time series of ocean kinetic energy, averaged within mixed layer depth of 40 m, revealed strong correspondence with the time series of area-integrated mean wind power, implying the dominant influence of local winds in driving the mean current. The geostrophic wind power also modulated the density surfaces, thereby influencing the APE except in mid–June. One explanation for such behaviour can be the arrival of downwelling Rossby waves associated with suppressed thermocline and thereby trying to negate the effects of winds. The variation in wind power led to generation of eddies in the region through baroclinic energy conversion (from APE to EKE).

It may be noted that the analyses presented here have certain limitations. The analysis in this study were carried out for only one year. Even though this general behavior of the SMC is similar every year, there can be considerable variability from year to year. Therefore, it is useful to carry out the analyses for a longer period using simple linear models as nonlinearities involved in our model may obscure several important features.

## Acknowledgments

This research was supported by Ministry of Human Resource Development (MHRD) funding. OSCAR data provided by NOAA-NASA ( [http://dx.doi.org/10.5067/ OSCAR-03D01](http://dx.doi.org/10.5067/OSCAR-03D01)), QuikSCAT winds by IFREMER (<http://www.ifremer.fr/cersat/en/data/ data.htm>) were used for the study. We sincerely thank Prof.J. P. McCreary for the insightful discussions. We also thank Dr. Zuojun Yu for her contributions in the work. Computations were carried out on a high performance computer (HPC) system facility funded by Department of Science and Technology under Fund for Improvement of ST Infrastructure in Universities and Higher Educational Institutions (FIST) scheme at Center for Atmospheric and Oceanic Sciences (CAOS), Indian Institute of Science, Bangalore and Divecha Center for Climate Change (DCCC). The authors are thankful to GFDL for providing the MOM4p1 source code. Ferret and Matlab has been used for data analysis and graphics output.

# Appendices

## A Background state

Let  $q$  be a model variable. Then, a key aspect of all our eddy analyses is the separation of  $q$  into mean (or slowly-varying)  $\bar{q}$  and time-varying  $q'$  ( $q = \bar{q} + q'$ ). Ideally, the mean (background) state should be free of high-frequency disturbances, that is, free from the influence of any eddies. We define  $\bar{q}$  to be the model field during 2009 smoothed by a 120-day, Lanczos low-pass filter, and  $q'$  to be the field obtained using a 120-day high-pass filter. We tried several cutoff periods, finding 120 days optimal: it is well above the residence period of mesoscale eddies in the region, and at the same time it retains the large-scale seasonal variability. The background state is the same for both eddy energy budget and TEM analysis.

## B TEM equations

### B.0.1 Equations of motion

The horizontal momentum and buoyancy equations can be decomposed into a mean and perturbation part as shown in (1). These equations under quasigeostrophic (QG) approximation in Reynold's averaged form become

$$\frac{\partial \bar{\mathbf{u}}_g}{\partial t} + \bar{\mathbf{u}}_g \cdot \nabla \bar{\mathbf{u}}_g + f_0 \mathbf{k} \times \bar{\mathbf{u}}_{ag} + \beta y \mathbf{k} \times \bar{\mathbf{u}}_g - \frac{\nabla \bar{p}_{ag}}{\rho_0} = \mathbf{G} - \nabla \cdot \overline{\mathbf{u}'\mathbf{u}'}, \quad (9)$$

$$\nabla_h \cdot \bar{\mathbf{u}}_{ag} + \frac{\partial \bar{w}_{ag}}{\partial z} = 0, \quad (10)$$

$$\frac{\partial \bar{b}}{\partial t} + \bar{\mathbf{u}}_g \cdot \nabla \bar{b} + \bar{w}_{ag} N_0^2 = X - \nabla \cdot \overline{\mathbf{u}'b'}, \quad (11)$$

where  $u_g$  represents geostrophic velocities, the overbar denotes the 120-day, low-pass-filtered background state and the primed quantities represent high-pass-filtered eddies.  $u_{ag}$ ,  $w_{ag}$  are the ageostrophic components,  $b$  represents the buoyancy and  $G$ ,  $X$  are forcing terms. Thus the effect of eddies on background state appear in two equations (Eqs. 9 and 11) represented by the convergence of eddy momentum fluxes,  $-\nabla \cdot \overline{\mathbf{u}'\mathbf{u}'}$  and buoyancy flux,  $-\nabla \cdot \overline{\mathbf{u}'b'}$ .

Apart from having an acceleration tendency on background flow, the momentum flux can also drive the horizontal mean ageostrophic flow. Also, the buoyancy fluxes can drive the mean flow implying the dynamical coupling between density and momentum equations. It is not thus possible to view how the density fluxes may accelerate or decelerate the background flow. Transformed Eulerian mean (TEM) approach helps us to get rid of this problem as a result of which only the eddy forcing appears in the horizontal momentum equations. The TEM equations can be written as

$$\frac{\partial \bar{\mathbf{u}}_g}{\partial t} + \bar{\mathbf{u}}_g \cdot \nabla \bar{\mathbf{u}}_g + f_0 \mathbf{k} \times \widetilde{\bar{\mathbf{u}}_{ag}} + \beta y \mathbf{k} \times \bar{\mathbf{u}}_g - \frac{\nabla \bar{p}_{ag}}{\rho_0} = \mathbf{G} - \underbrace{\nabla \cdot \mathbf{E}}_{EF}, \quad (12)$$

$$\nabla_h \cdot \widetilde{\mathbf{u}}_{ag} + \frac{\partial \widetilde{w}_{ag}}{\partial z} = 0, \quad (13)$$

$$\frac{\partial \bar{b}}{\partial t} + \overline{\mathbf{u}}_g \cdot \nabla \bar{b} + \widetilde{w}_{ag} N_0^2 = X \quad (14)$$

where  $EF$  = eddy forcing. The tilde over the ageostrophic circulation terms represents the residual mean circulation. In many cases, the mean ageostrophic circulation can negate the impact of eddies. The residual mean circulation represents the net effect of the two quantities. Eddy components are given by the eddy bolus velocities,

$$\mathbf{u}^* = -\frac{\partial \overline{b'\mathbf{u}'}}{\partial z N_0^2}, \quad \mathbf{w}^* = \nabla \cdot \frac{\overline{b'\mathbf{u}'}}{N_0^2}. \quad (15)$$

## C Eddy potential vorticity flux

Vector  $\mathbf{E}$  in (12) represents the eddy-stress tensor (Plumb, 1986). The advantage of using the QG approximation to understand eddy-driven mean flows is that it expresses the divergence of eddy stress tensor explicitly in terms of eddy potential-vorticity flux.

$$\nabla \cdot \mathbf{E} \approx -\hat{\mathbf{k}} \times \overline{q'\mathbf{u}'}, \quad (16)$$

where

$$q'\mathbf{u}' = \nabla \cdot \begin{pmatrix} N & M - P & 0 \\ M - P & -N & 0 \\ R & S & 0 \end{pmatrix}, \quad (17)$$

$M = (\overline{v'^2 - u'^2})/2$ ,  $N = \overline{u'v'}$ ,  $P = (\overline{b'^2}/2) N^2$ ,  $R = \overline{v'b'}$ , and  $S = (f_0/N_0^2) \overline{u'b'}$ . Variables  $M$  and  $N$  are the eddy momentum flux,  $P$  is the eddy potential energy, and  $R$  and  $S$  are the meridional and zonal eddy buoyancy fluxes under the QG assumption. Although both eddy momentum and buoyancy fluxes impact the mean flow, considering their effects separately can sometimes be misleading. This problem is avoided in  $\mathbf{E}$ , which combines the influence of the two fluxes. The component of  $\mathbf{E}$  normal to the mean flow tends to accelerate or decelerate it, whereas the component parallel to the mean flow tends to turn it.



## References

- Brown, J. N. and Fedorov, A. V. (2010). How much energy is transferred from the winds to the thermocline on enso time scales? *Journal of Climate*, 23(6):1563–1580.
- Chassignet, E. P. and Garraffo, Z. D. (2001). Viscosity parameterization and the gulf stream separation. Technical report, DTIC Document.
- Chen, G., Wang, D., and Hou, Y. (2012). The features and interannual variability mechanism of mesoscale eddies in the bay of bengal. *Continental Shelf Research*, 47:178–185.
- Cheng, X., McCreary, J. P., Qiu, B., Qi, Y., and Du, Y. (2017). Intraseasonal-to-semiannual variability of sea-surface height in the eastern, equatorial indian ocean and southern bay of bengal. *Journal of Geophysical Research: Oceans*.
- Cheng, X., Xie, S.-P., McCreary, J. P., Qi, Y., and Du, Y. (2013). Intraseasonal variability of sea surface height in the bay of bengal. *Journal of Geophysical Research: Oceans*, 118(2):816–830.
- Das, U., Vinayachandran, P., and Behara, A. (2015). Formation of the southern bay of bengal cold pool. *Climate Dynamics*, pages 1–15.
- Hastenrath, S. and Greischar, L. (1991). The monsoonal current regimes of the tropical indian ocean: Observed surface flow fields and their geostrophic and wind-driven components. *Journal of Geophysical Research: Oceans*, 96(C7):12619–12633.
- Holland, W. R. and Rhines, P. B. (1980). An example of eddy-induced ocean circulation. *Journal of Physical Oceanography*, 10(7):1010–1031.
- Huang, R. X. (2005). Available potential energy in the world’s oceans. *Journal of Marine Research*, 63(1):141–158.
- Huang, R. X. (2010). *Ocean circulation: wind-driven and thermohaline processes*. Cambridge University Press.
- Ikeda, M. (1981). Meanders and detached eddies of a strong eastward-flowing jet using a two-layer quasi-geostrophic model. *Journal of Physical Oceanography*, 11(4):526–540.
- Jackett, D. R., McDougall, T. J., Feistel, R., Wright, D. G., and Griffies, S. M. (2006). Algorithms for density, potential temperature, conservative temperature, and the freezing temperature of seawater. *Journal of Atmospheric and Oceanic Technology*, 23(12):1709–1728.
- Jensen, T. G. (2001). Arabian sea and bay of bengal exchange of salt and tracers in an ocean model. *Geophys. Res. Lett*, 28(20):3967–3970.

- Jensen, T. G., Wijesekera, H. W., Nyadjro, E. S., Thoppil, P. G., Shriver, J. F., Sandeep, K., and Pant, V. (2016). Modeling salinity exchanges between the equatorial indian ocean and the bay of bengal. *Oceanography*, 29(2):92–101.
- Kurian, J. and Vinayachandran, P. (2007). Mechanisms of formation of the arabian sea mini warm pool in a high-resolution ocean general circulation model. *Journal of Geophysical Research: Oceans*, 112(C5).
- Large, W. G., McWilliams, J. C., and Doney, S. C. (1994). Oceanic vertical mixing: A review and a model with a nonlocal boundary layer parameterization. *Reviews of Geophysics*, 32(4):363–403.
- Lee, C. M., Jinadasa, S., Anutaliya, A., Centurioni, L. R., Fernando, H. J., Hormann, V., Lankhorst, M., Rainville, L., Send, U., and Wijesekera, H. W. (2016). Collaborative observations of boundary currents, water mass variability, and monsoon response in the southern bay of bengal. *Oceanography*, 29(2):102–111.
- Lee, I., Liu, J. T., et al. (2006). Rectification of the heading and tilting of sediment trap arrays due to strong tidal currents in a submarine canyon. *Geophysical research letters*, 33(8).
- Masina, S., Philander, S., and Bush, A. (1999). An analysis of tropical instability waves in a numerical model of the pacific ocean: 2. generation and energetics of the waves. *Journal of Geophysical Research: Oceans*, 104(C12):29637–29661.
- McCreary, J., Han, W., Shankar, D., and Shetye, S. (1996). Dynamics of the east india coastal current: 2. numerical solutions. *Journal of Geophysical Research: Oceans*, 101(C6):13993–14010.
- Molinari, R. L., Olson, D., and Reverdin, G. (1990). Surface current distributions in the tropical indian ocean derived from compilations of surface buoy trajectories. *Journal of Geophysical Research: Oceans*, 95(C5):7217–7238.
- Murty, V., Sarma, Y., Rao, D., and Murty, C. (1992). Water characteristics, mixing and circulation in the bay of bengal during southwest monsoon. *Journal of Marine Research*, 50(2):207–228.
- Oort, A. H., Ascher, S. C., Levitus, S., and Peixóto, J. P. (1989). New estimates of the available potential energy in the world ocean. *Journal of Geophysical Research: Oceans*, 94(C3):3187–3200.
- Plumb, R. A. (1986). Three-dimensional propagation of transient quasi-geostrophic eddies and its relationship with the eddy forcing of the time-mean flow. *Journal of the atmospheric sciences*, 43(16):1657–1678.

- Schott, F., Reppin, J., Fischer, J., and Quadfasel, D. (1994). Currents and transports of the monsoon current south of sri lanka. *Journal of Geophysical Research: Oceans*, 99(C12):25127–25141.
- Schott, F. A. and McCreary, J. P. (2001). The monsoon circulation of the indian ocean. *Progress in Oceanography*, 51(1):1–123.
- Shankar, D., McCreary, J., Han, W., and Shetye, S. (1996). Dynamics of the east india coastal current: 1. analytic solutions forced by interior ekman pumping and local alongshore winds. *Journal of Geophysical Research: Oceans*, 101(C6):13975–13991.
- Shankar, D., Vinayachandran, P., and Unnikrishnan, A. (2002). The monsoon currents in the north indian ocean. *Progress in oceanography*, 52(1):63–120.
- Shenoi, S., Saji, P., and Almeida, A. (1999). Near-surface circulation and kinetic energy in the tropical indian ocean derived from lagrangian drifters. *Journal of Marine Research*, 57(6):885–907.
- Simmons, H. L., Jayne, S. R., Laurent, L. C. S., and Weaver, A. J. (2004). Tidally driven mixing in a numerical model of the ocean general circulation. *Ocean Modelling*, 6(3):245–263.
- Sindhu, B., Suresh, I., Unnikrishnan, A., Bhatkar, N., Neetu, S., and Michael, G. (2007). Improved bathymetric datasets for the shallow water regions in the indian ocean. *Journal of Earth System Science*, 116(3):261–274.
- Vinayachandran, P., Masumoto, Y., Yamagata, T., and Mikawa, T. (1999). Intrusion of the southwest monsoon current into the bay of bengal. *Journal of Geophysical Research*, 104(C5):11077–11085.
- Vinayachandran, P., Neema, C., Mathew, S., and Remya, R. (2012). Mechanisms of summer intraseasonal sea surface temperature oscillations in the bay of bengal. *Journal of Geophysical Research: Oceans*, 117(C1).
- Vinayachandran, P., Shankar, D., Vernekar, S., Sandeep, K., Amol, P., Neema, C., and Chatterjee, A. (2013). A summer monsoon pump to keep the bay of bengal salty. *Geophysical Research Letters*, 40(9):1777–1782.
- Vinayachandran, P. and Yamagata, T. (1998). Monsoon response of the sea around sri lanka: generation of thermal domes and anticyclonic vortices. *Journal of Physical Oceanography*, 28(10):1946–1960.
- Wilson, C. and Williams, R. G. (2004). Why are eddy fluxes of potential vorticity difficult to parameterize? *Journal of physical oceanography*, 34(1):142–155.

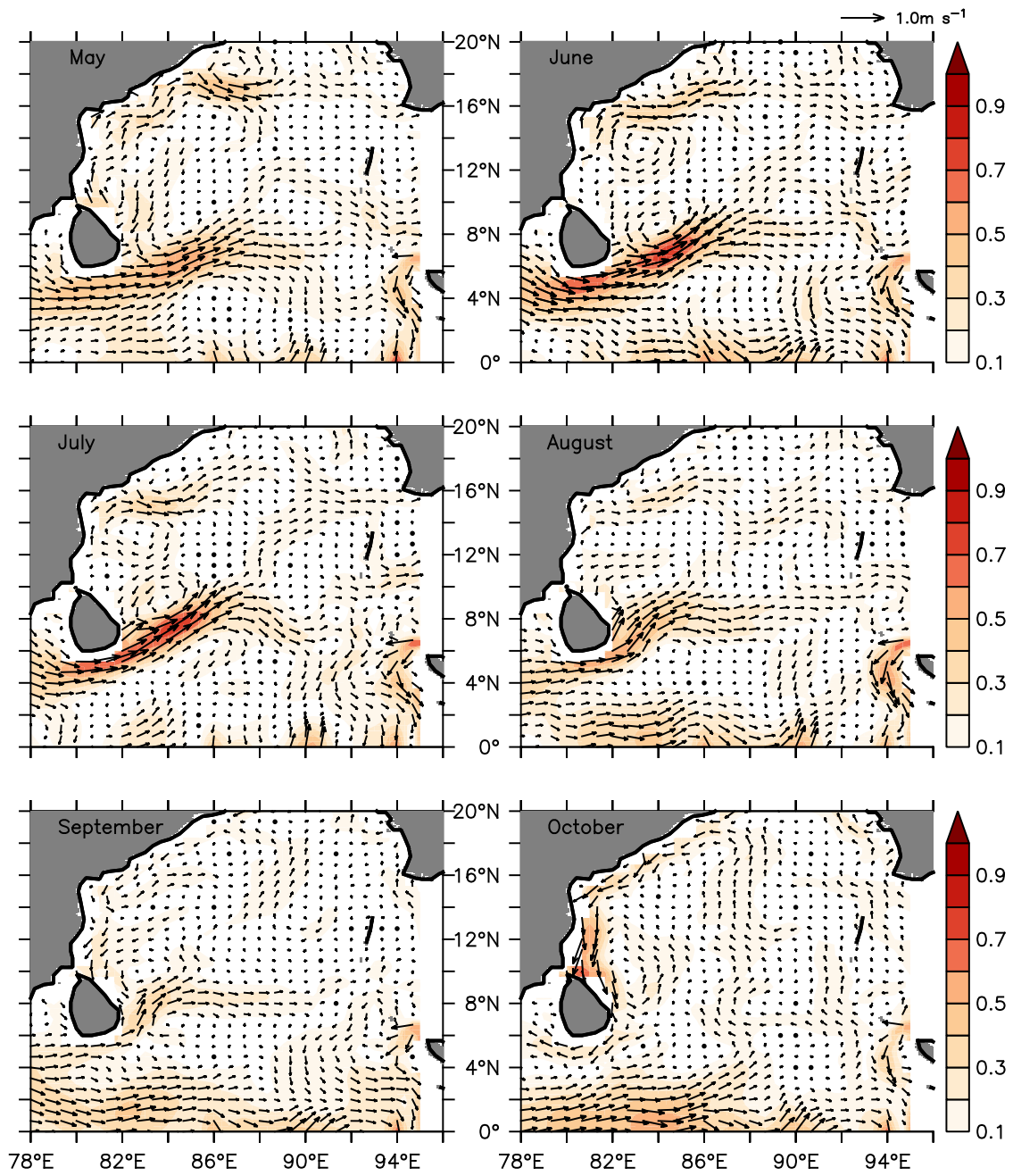


Figure 1: Monthly maps of climatological (2000–2009) currents from OSCAR averaged from May–October. The scale vector (1 m/s) is shown above panel.

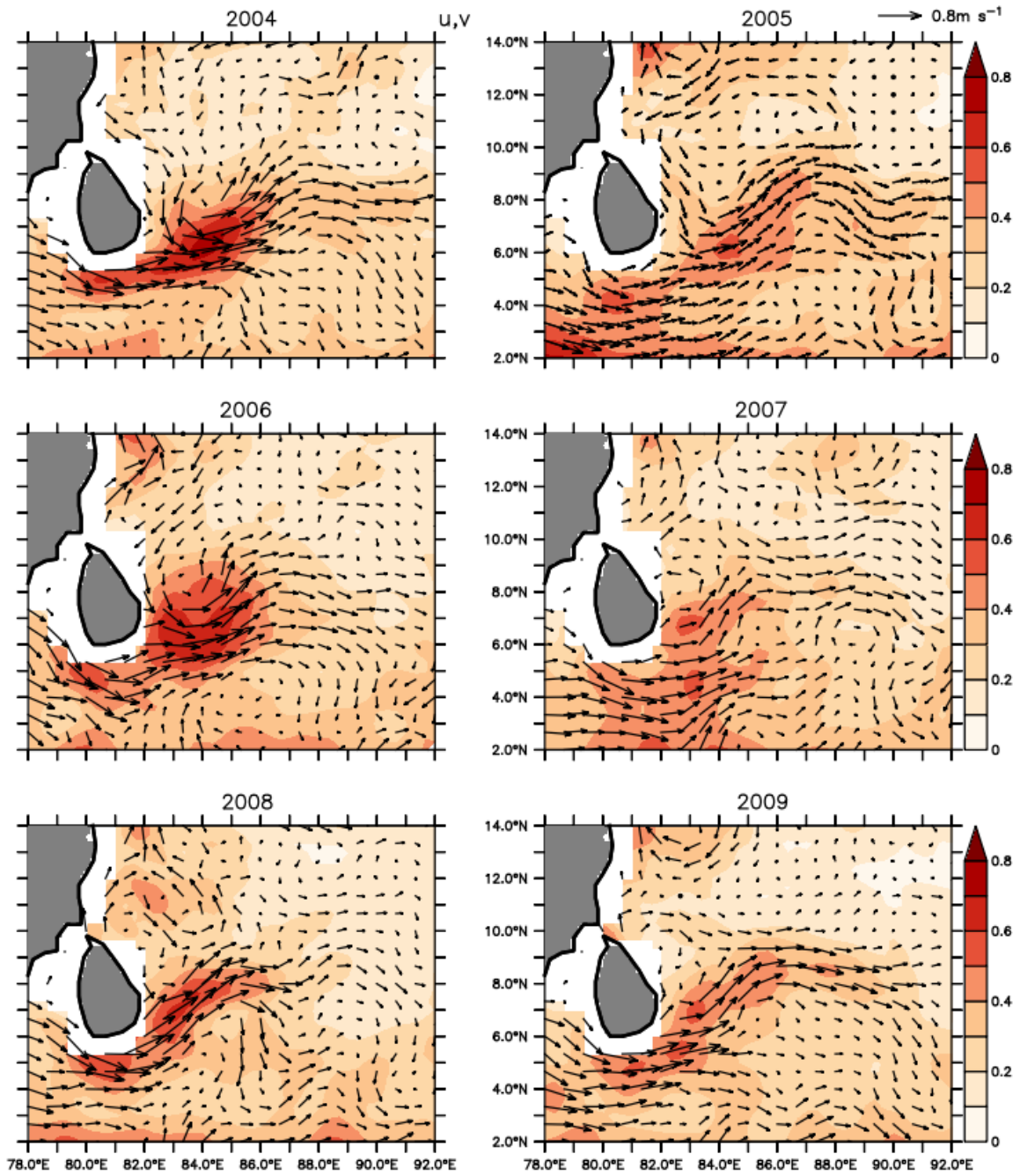


Figure 2: Time mean (June– September) circulation map of SMC from 2004–2009. The scale vector (0.8 m/s) is shown above panel.

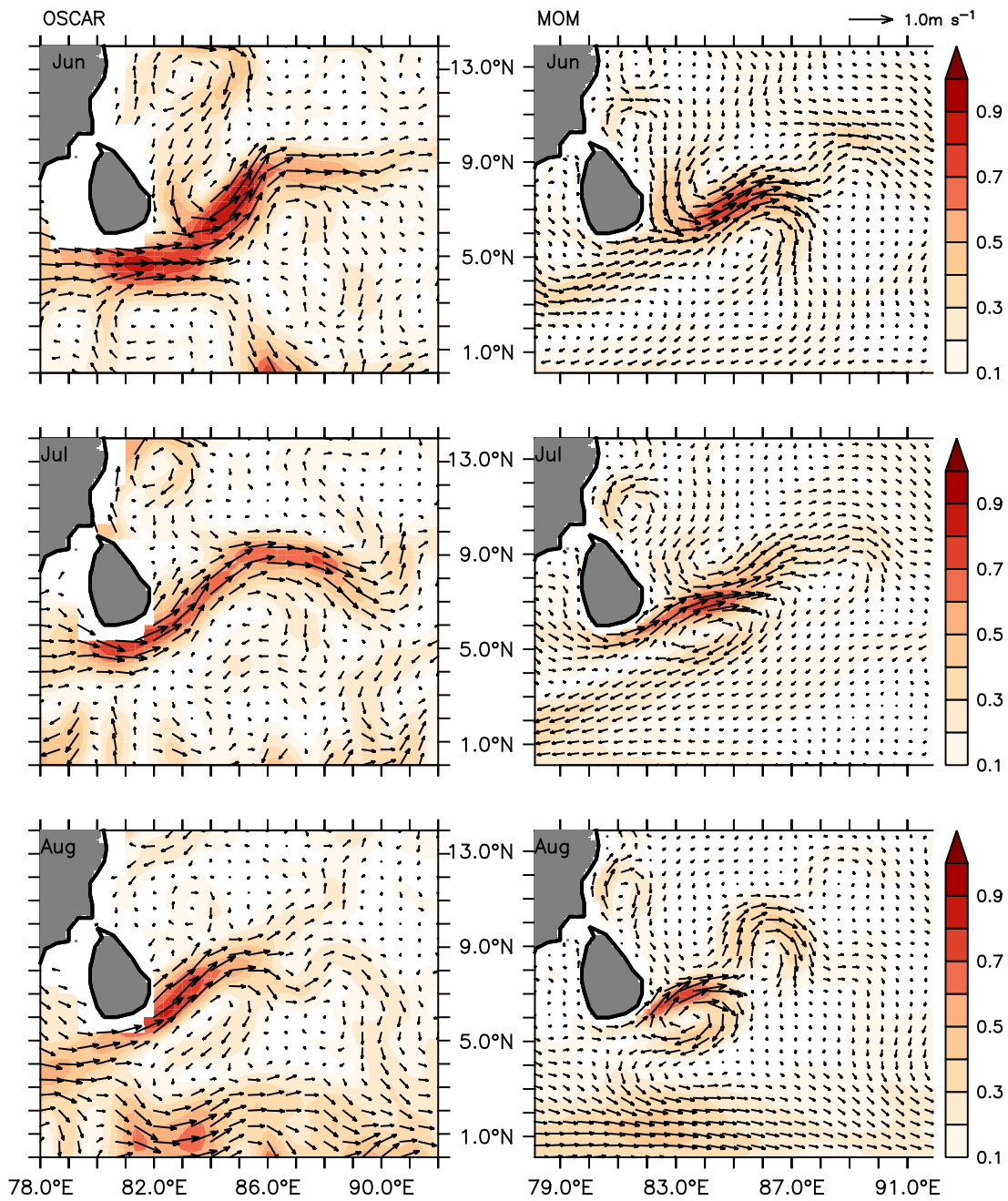


Figure 3: Comparison of monthly maps of currents of southwest monsoon, 2009 from OSCAR (left panels), MOM (right panels). Current vectors overlaid over speed (shading, cm/s). Vectors are of same length in all panels and the scale vector (1m/s) is shown above panel.

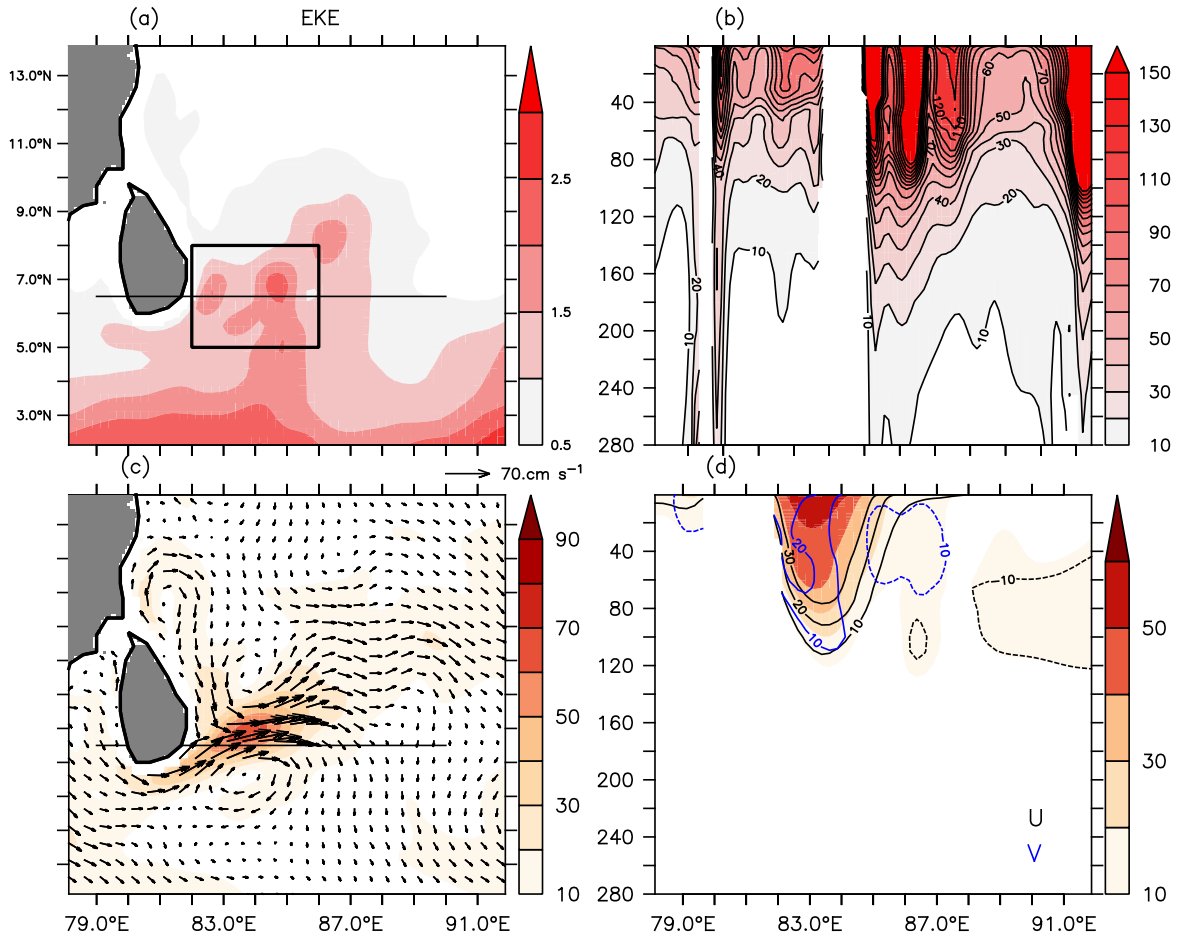


Figure 4: (a) Time mean (June-September) vertically integrated EKE map ( $\text{cm}^3/\text{s}^2$ ); (b) depth longitude section along  $6.5^\circ\text{N}$  of time mean (Jun-Sep) EKE ( $10^{-4} \text{ cm}^2/\text{s}^2$ ). Vectors are of length  $60 \text{ cm/s}$ . (c) Time mean (June-September) maps of surface averaged ( $30\text{m}$ ) current vectors from the model overlaid over speed (shading  $\text{cm/s}$ ); (d) time mean depth longitude sections ( $6.5^\circ\text{N}$ ) of zonal velocity (red), meridional velocity (blue) contour spacing of  $10\text{cm/s}$  overlaid over speed of current ( $\text{cm/s}$ ).

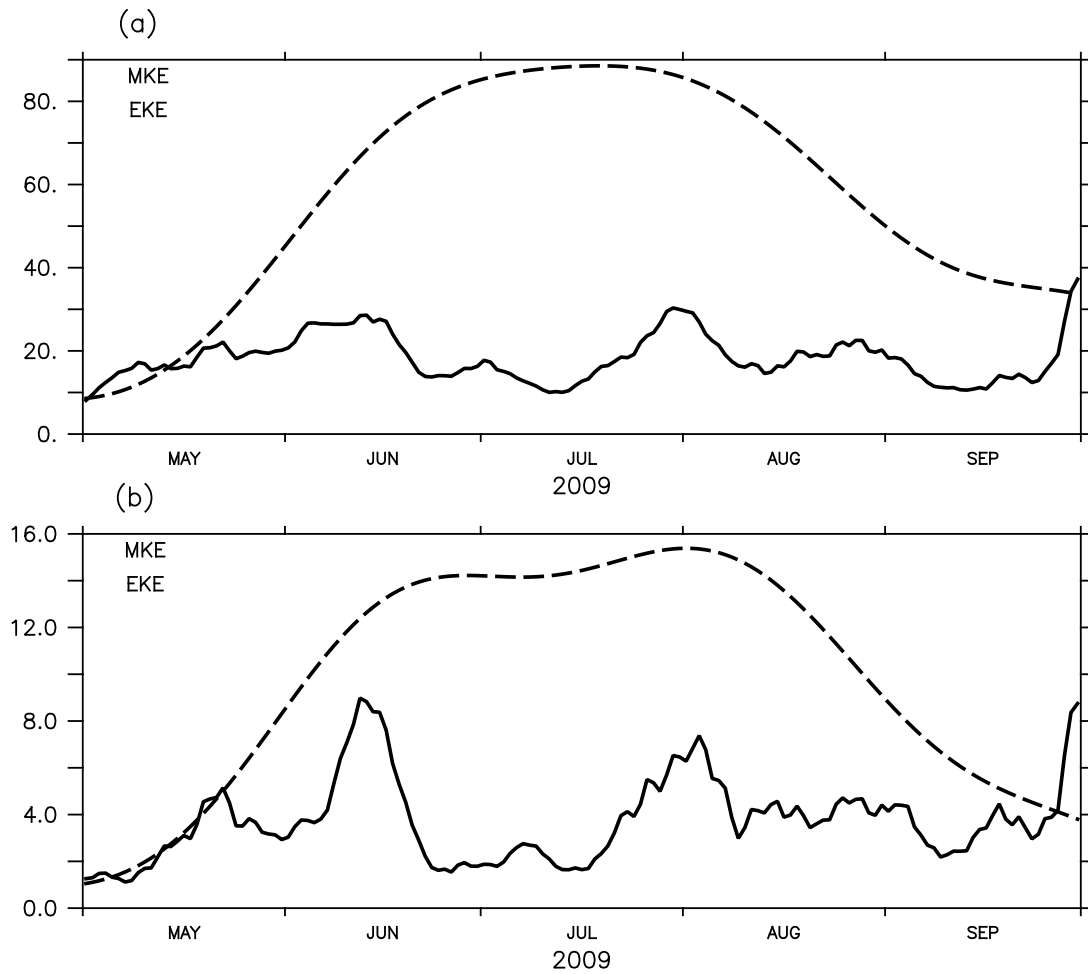


Figure 5: (a) A volume integrated time MKE (dashed lines) and EKE (solid lines) between 82–86°E, 5–8°N, 0–100m. Units– ( $10^{16} cm^2/s^2$ ); (b) volume integrated time MKE and EKE between 84–85°E and 5–7°N.



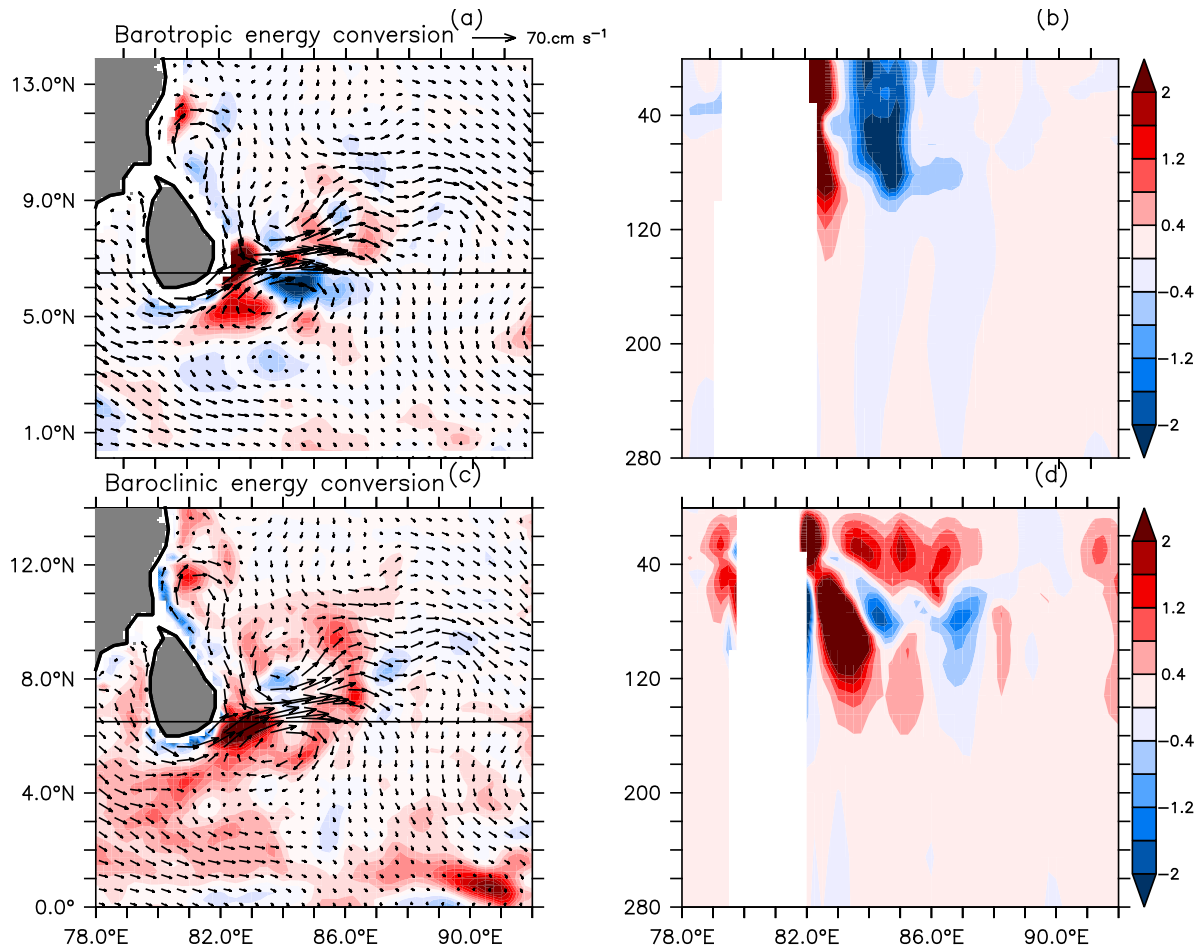


Figure 6: Time mean (June–September) vertically integrated (0–100 m) map of (a) barotropic; (c) baroclinic energy conversion terms ( $\text{cm}^3/\text{s}^3$ ). Time mean depth longitude sections ( $10^{-4} \text{ cm}^2/\text{s}^3$ ) of (b) barotropic energy conversion, (d) baroclinic energy conversion at  $6.5^\circ\text{N}$ . Time mean current vectors are averaged over 50 m are of same scale ( $0.6\text{m/s}$ ) in both panels.

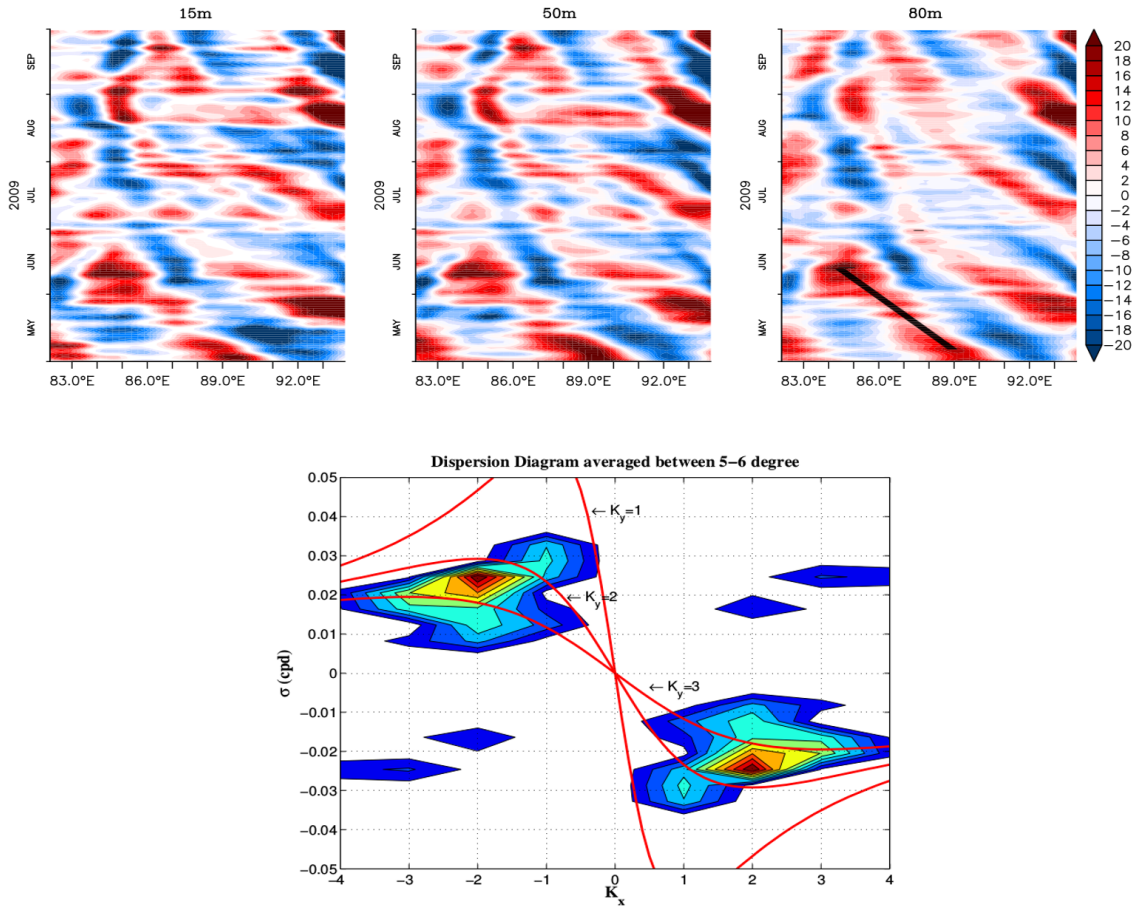


Figure 7: Hovmöller diagram (top) of high passed filtered meridional velocities averaged from 5–6°N. Levels 15 m, 50 m, 80 m. Dispersion diagram (bottom) frequency ( $\sigma$ ) versus wavenumber ( $k$ ).

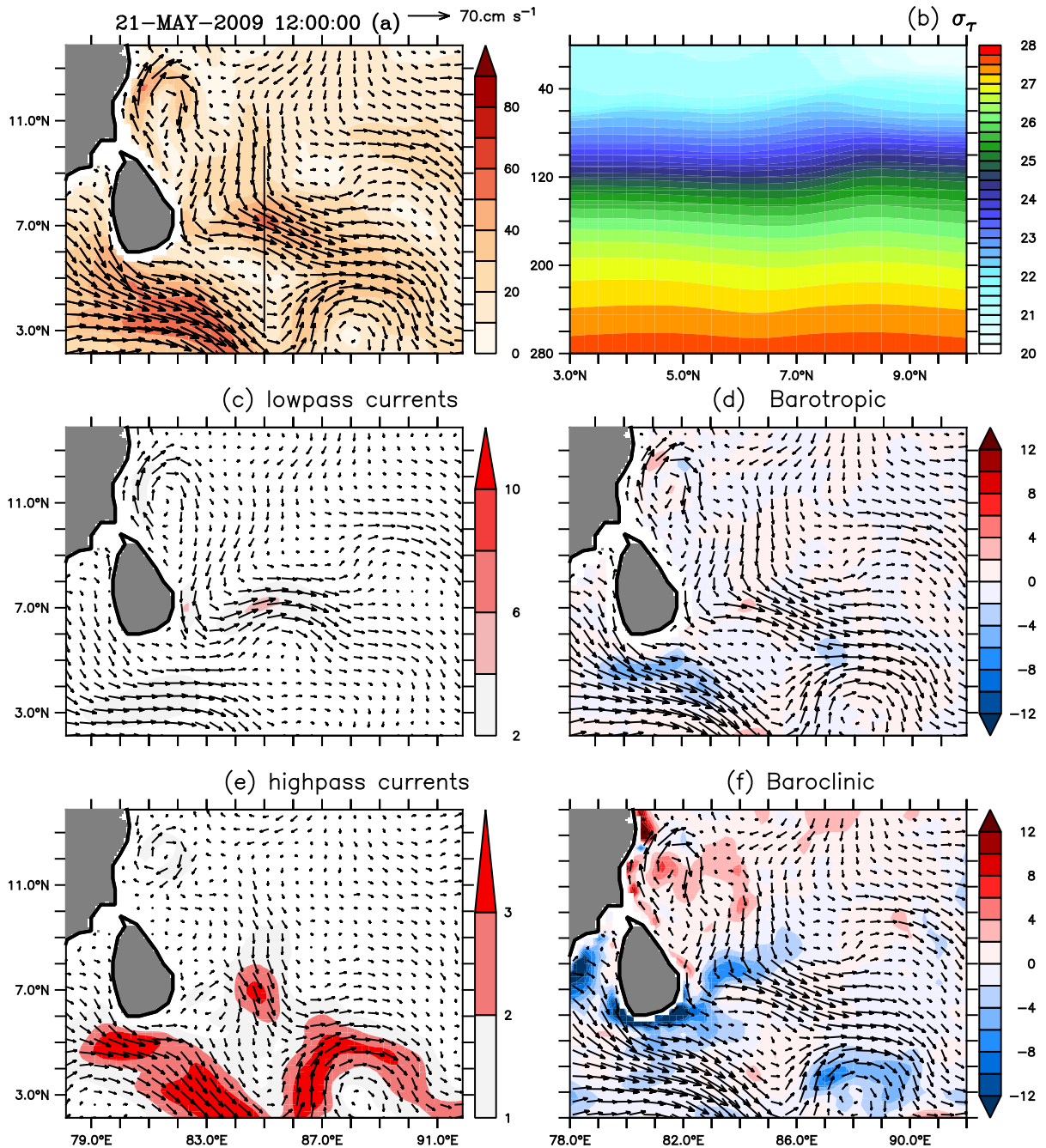


Figure 8: (a) Current vectors overlaid over speed (shading, cm/s) averaged over top 30m; (b)  $\sigma_t$  ( $\text{kg/m}^3$ ); (c) 120 day lowpass filtered currents (top 30m depth averaged) as mean flow overlaid over top 100 m vertically integrated map of MKE (shading,  $\text{cm}^3/\text{s}^2$ ); (d) Current vectors (top 30m depth averaged) overlaid over top 100 m vertically integrated map of barotropic energy conversion  $-u'_i u'_j \partial \bar{u}_i / \partial y$  (shading,  $\text{cm}^3/\text{s}^3$ ); (e) 120 day highpass filtered currents (cm/s) averaged over top 30 m, as eddies overlaid over top 100 m vertically integrated map of EKE (shading,  $10^6 \text{ cm}^3/\text{s}^2$ ); (f) Current vectors (top 30m depth averaged) overlaid over top 100 m vertically integrated map of baroclinic energy conversion (shading,  $\text{cm}^3/\text{s}^3$ ). All quantities are 5-day running averaged. Vectors are of same length in all panels and the scale vector is shown in above panel (a).

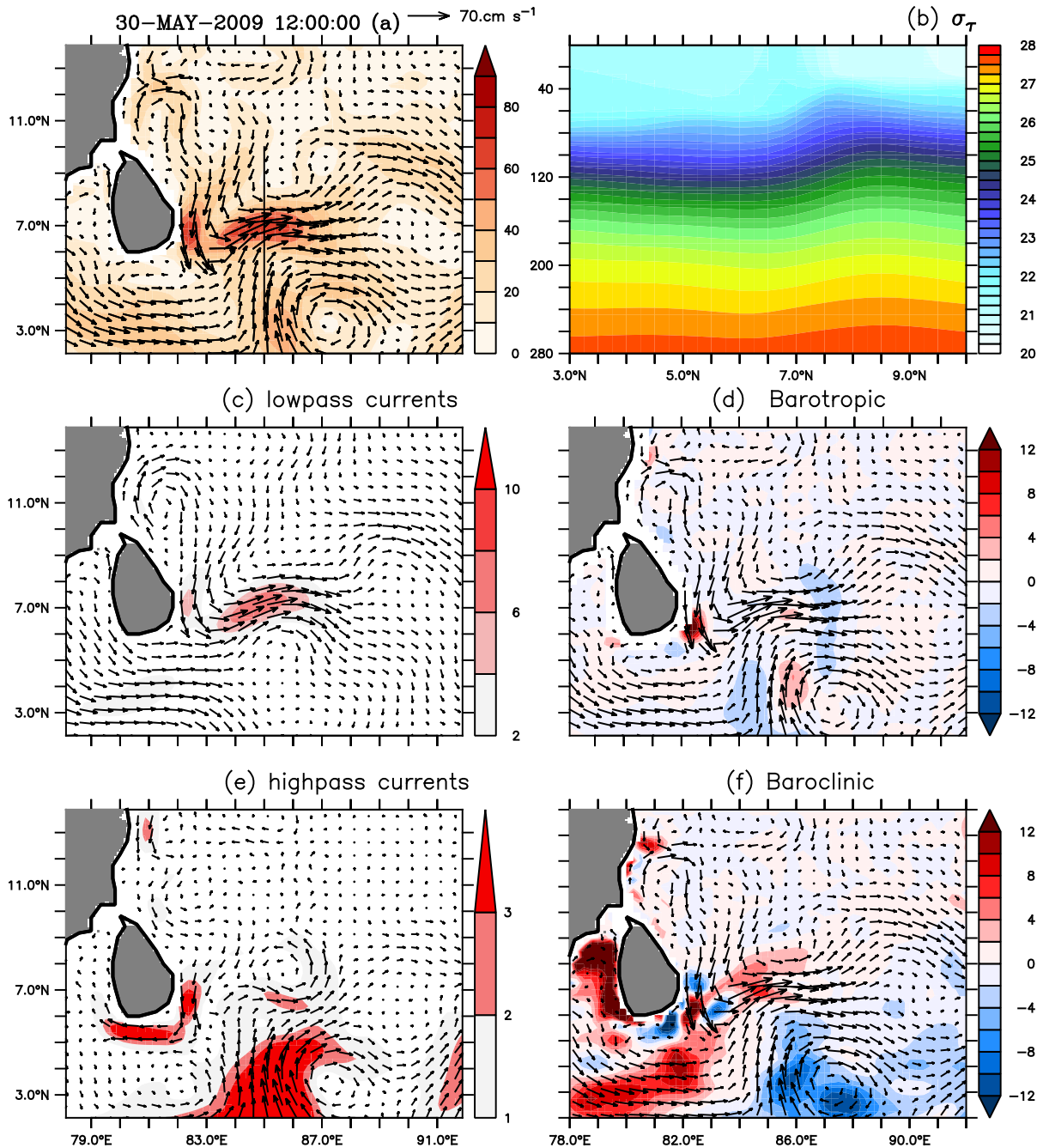


Figure 9: (a) Current vectors overlaid over speed (shading, cm/s) averaged over top 30m; (b)  $\sigma_t$  ( $\text{kg/m}^3$ ); (c) 120 day lowpass filtered currents (top 30m depth averaged) as mean flow overlaid over top 100 m vertically integrated map of MKE (shading,  $\text{cm}^3/\text{s}^2$ ); (d) Current vectors (top 30m depth averaged) overlaid over top 100 m vertically integrated map of barotropic energy conversion  $-u'_i u'_j \partial \bar{u}_i / \partial y$  (shading,  $\text{cm}^3/\text{s}^3$ ); (e) 120 day highpass filtered currents (cm/s) averaged over top 30 m, as eddies overlaid over top 100 m vertically integrated map of EKE (shading,  $10^6 \text{ cm}^3/\text{s}^2$ ); (f) Current vectors (top 30m depth averaged) overlaid over top 100 m vertically integrated map of baroclinic energy conversion (shading,  $\text{cm}^3/\text{s}^3$ ). All quantities are 5-day running averaged. Vectors are of same length in all panels and the scale vector is shown in above panel (a).

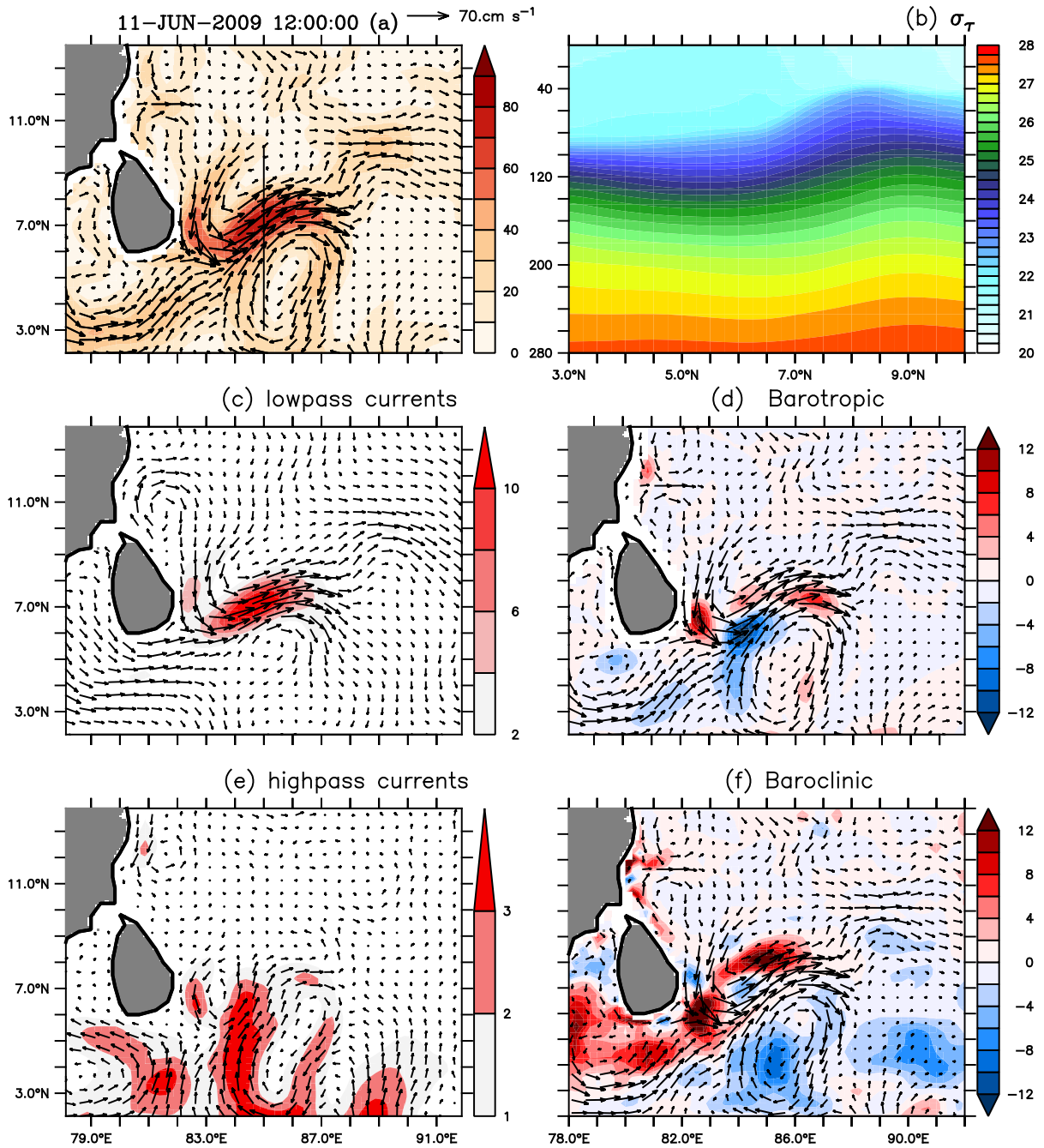


Figure 10: (a) Current vectors overlaid over speed (shading, cm/s) averaged over top 30m; (b)  $\sigma_t$  ( $\text{kg/m}^3$ ); (c) 120 day lowpass filtered currents (top 30m depth averaged) as mean flow overlaid over top 100 m vertically integrated map of MKE (shading,  $\text{cm}^3/\text{s}^2$ ); (d) Current vectors (top 30m depth averaged) overlaid over top 100 m vertically integrated map of barotropic energy conversion  $-u'_i u'_j \partial \bar{u}_i / \partial y$  (shading,  $\text{cm}^3/\text{s}^3$ ); (e) 120 day highpass filtered currents (cm/s) averaged over top 30 m, as eddies overlaid over top 100 m vertically integrated map of EKE (shading,  $10^6 \text{ cm}^3/\text{s}^2$ ); (f) Current vectors (top 30m depth averaged) overlaid over top 100 m vertically integrated map of baroclinic energy conversion (shading,  $\text{cm}^3/\text{s}^3$ ). All quantities are 5-day running averaged. Vectors are of same length in all panels and the scale vector is shown in above panel (a).

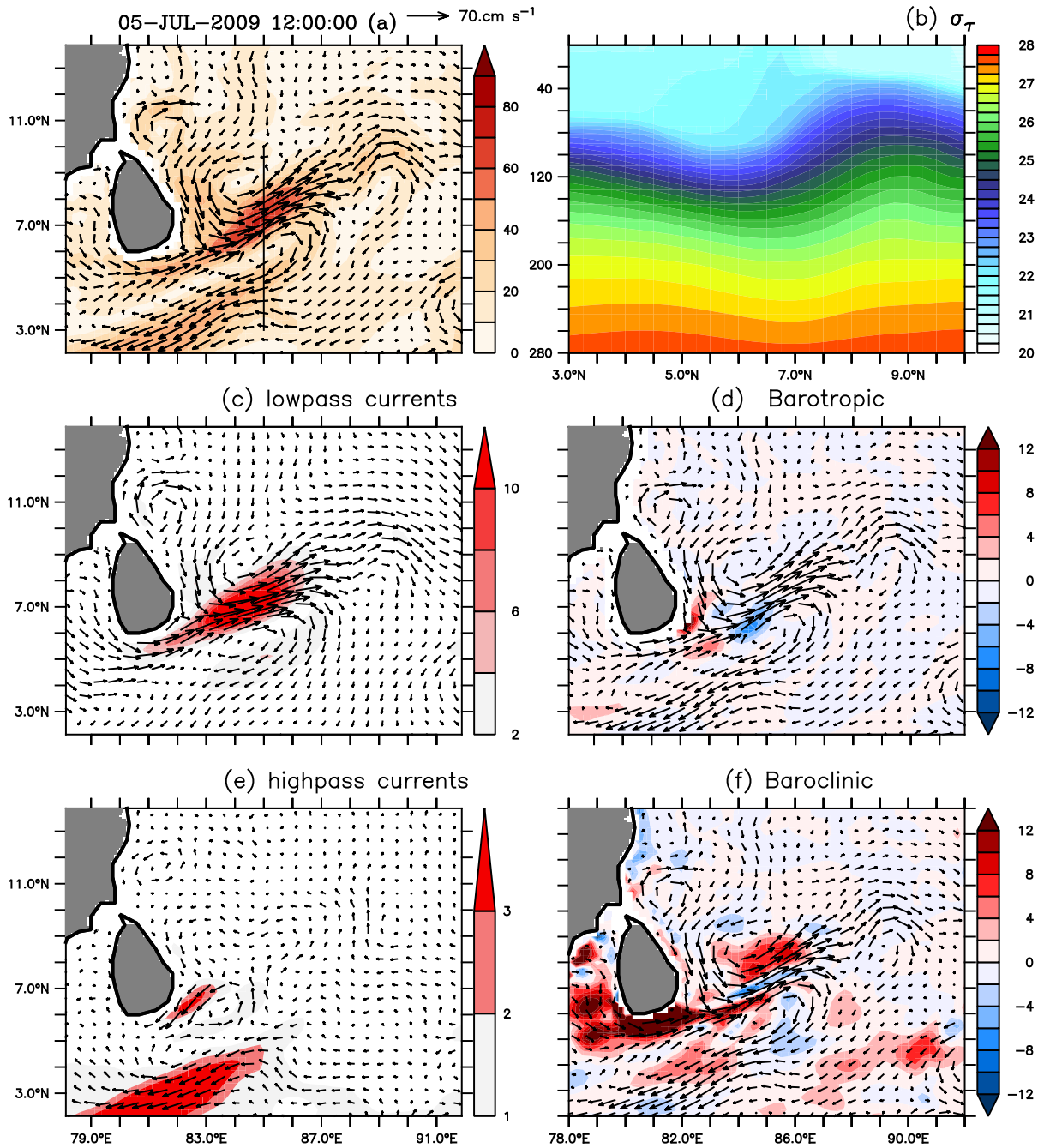


Figure 11: (a) Current vectors overlaid over speed (shading, cm/s) averaged over top 30m; (b)  $\sigma_t$  ( $\text{kg/m}^3$ ); (c) 120 day lowpass filtered currents (top 30m depth averaged) as mean flow overlaid over top 100 m vertically integrated map of MKE (shading,  $\text{cm}^3/\text{s}^2$ ); (d) Current vectors (top 30m depth averaged) overlaid over top 100 m vertically integrated map of barotropic energy conversion  $-u'_i u'_j \partial \bar{u}_i / \partial y$  (shading,  $\text{cm}^3/\text{s}^3$ ); (e) 120 day highpass filtered currents (cm/s) averaged over top 30 m, as eddies overlaid over top 100 m vertically integrated map of EKE (shading,  $10^6 \text{ cm}^3/\text{s}^2$ ); (f) Current vectors (top 30m depth averaged) overlaid over top 100 m vertically integrated map of baroclinic energy conversion (shading,  $\text{cm}^3/\text{s}^3$ ). All quantities are 5-day running averaged. Vectors are of same length in all panels and the scale vector is shown in above panel (a).

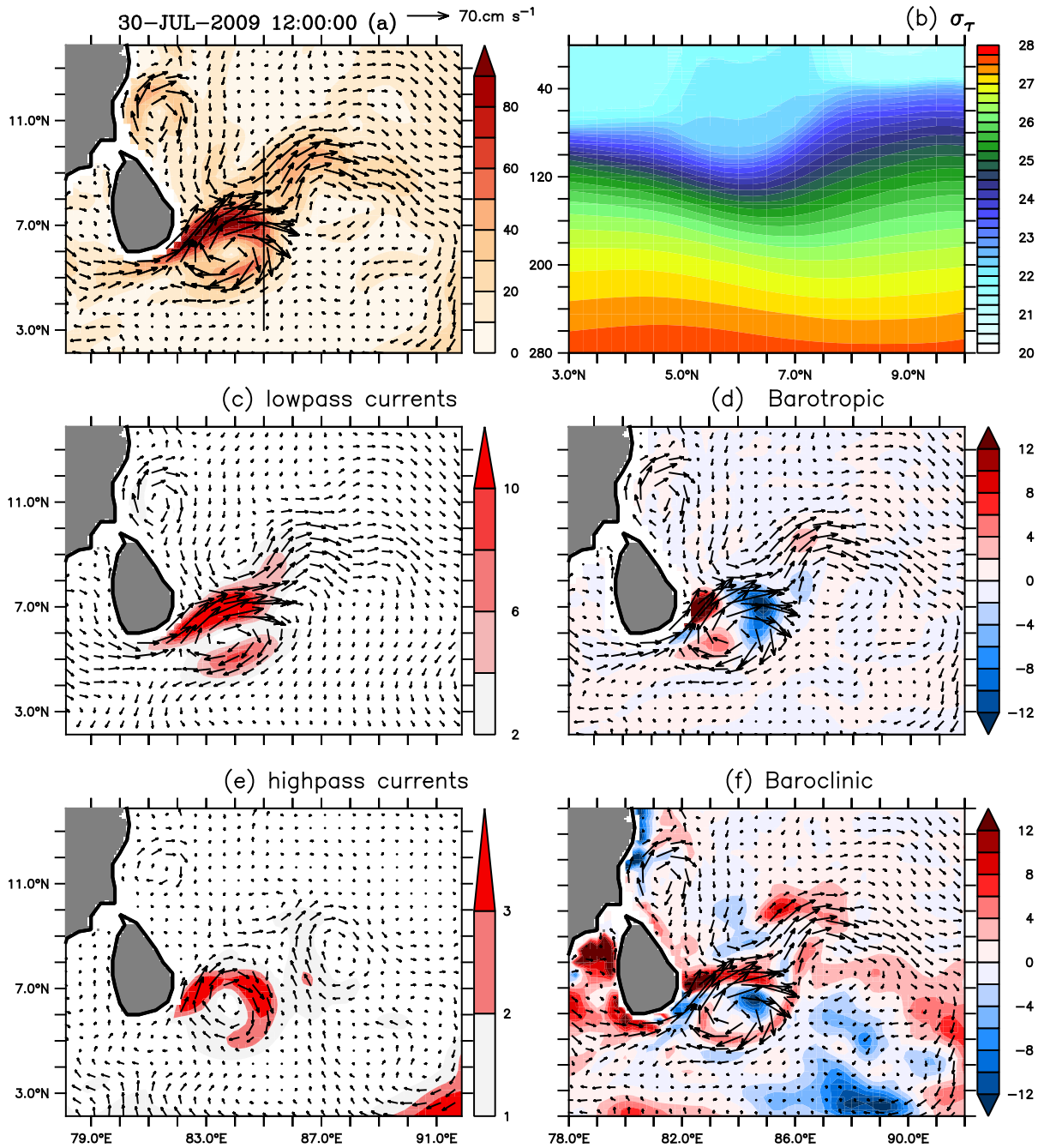


Figure 12: (a) Current vectors overlaid over speed (shading, cm/s) averaged over top 30m; (b)  $\sigma_t$  ( $\text{kg/m}^3$ ); (c) 120 day lowpass filtered currents (top 30m depth averaged) as mean flow overlaid over top 100 m vertically integrated map of MKE (shading,  $\text{cm}^3/\text{s}^2$ ); (d) Current vectors (top 30m depth averaged) overlaid over top 100 m vertically integrated map of barotropic energy conversion  $-u'_i u'_j \partial \bar{u}_i / \partial y$  (shading,  $\text{cm}^3/\text{s}^3$ ); (e) 120 day highpass filtered currents (cm/s) averaged over top 30 m, as eddies overlaid over top 100 m vertically integrated map of EKE (shading,  $10^6 \text{ cm}^3/\text{s}^2$ ); (f) Current vectors (top 30m depth averaged) overlaid over top 100 m vertically integrated map of baroclinic energy conversion (shading,  $\text{cm}^3/\text{s}^3$ ). All quantities are 5-day running averaged. Vectors are of same length in all panels and the scale vector is shown in above panel (a).

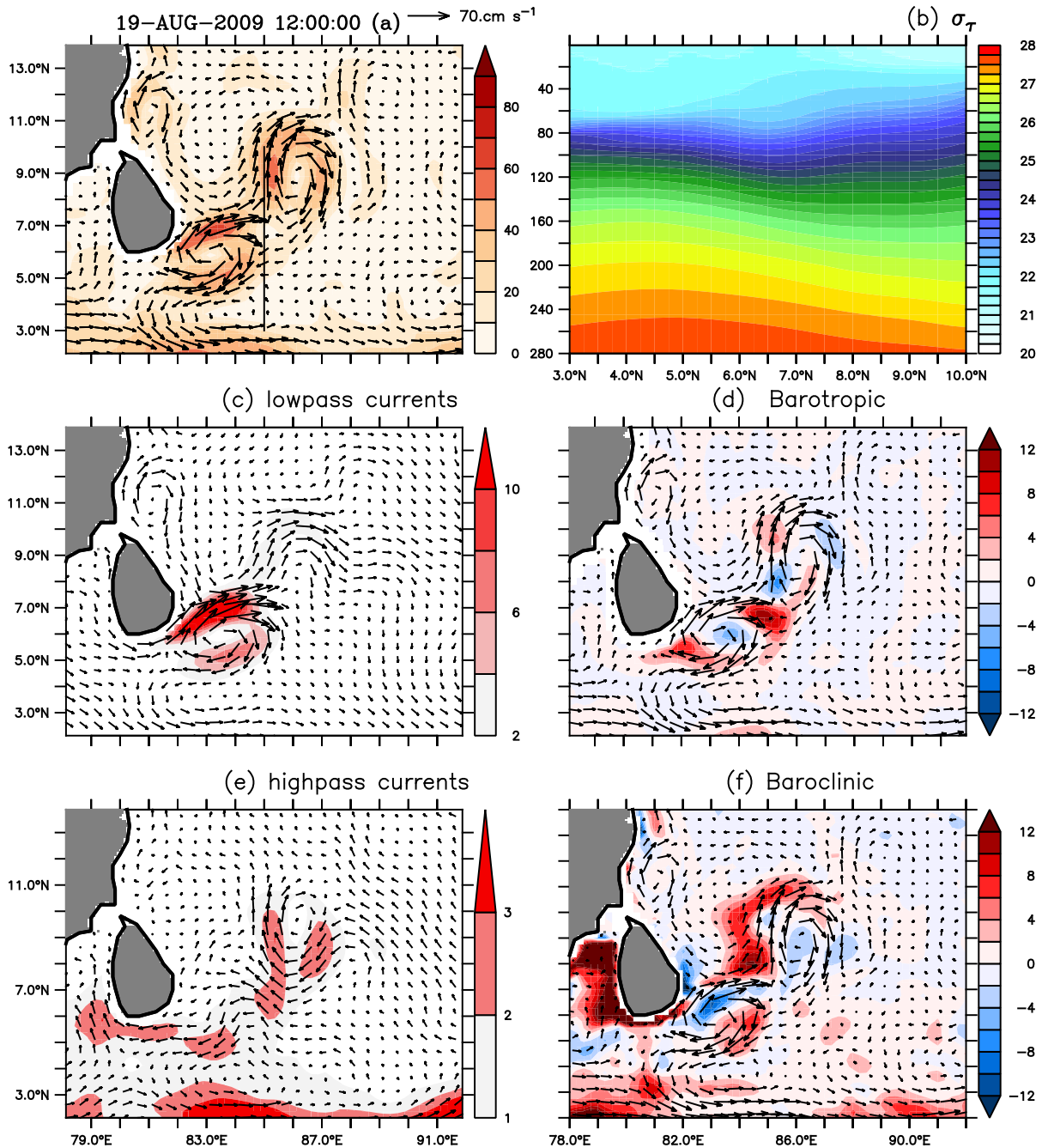


Figure 13: (a) Current vectors overlaid over speed (shading, cm/s) averaged over top 30m; (b)  $\sigma_t$  ( $\text{kg/m}^3$ ); (c) 120 day lowpass filtered currents (top 30m depth averaged) as mean flow overlaid over top 100 m vertically integrated map of MKE (shading,  $\text{cm}^3/\text{s}^2$ ); (d) Current vectors (top 30m depth averaged) overlaid over top 100 m vertically integrated map of barotropic energy conversion  $-u'_i u'_j \partial \bar{u}_i / \partial y$  (shading,  $\text{cm}^3/\text{s}^3$ ); (e) 120 day highpass filtered currents (cm/s) averaged over top 30 m, as eddies overlaid over top 100 m vertically integrated map of EKE (shading,  $10^6 \text{ cm}^3/\text{s}^2$ ); (f) Current vectors (top 30m depth averaged) overlaid over top 100 m vertically integrated map of baroclinic energy conversion (shading,  $\text{cm}^3/\text{s}^3$ ). All quantities are 5-day running averaged. Vectors are of same length in all panels and the scale vector is shown in above panel (a).



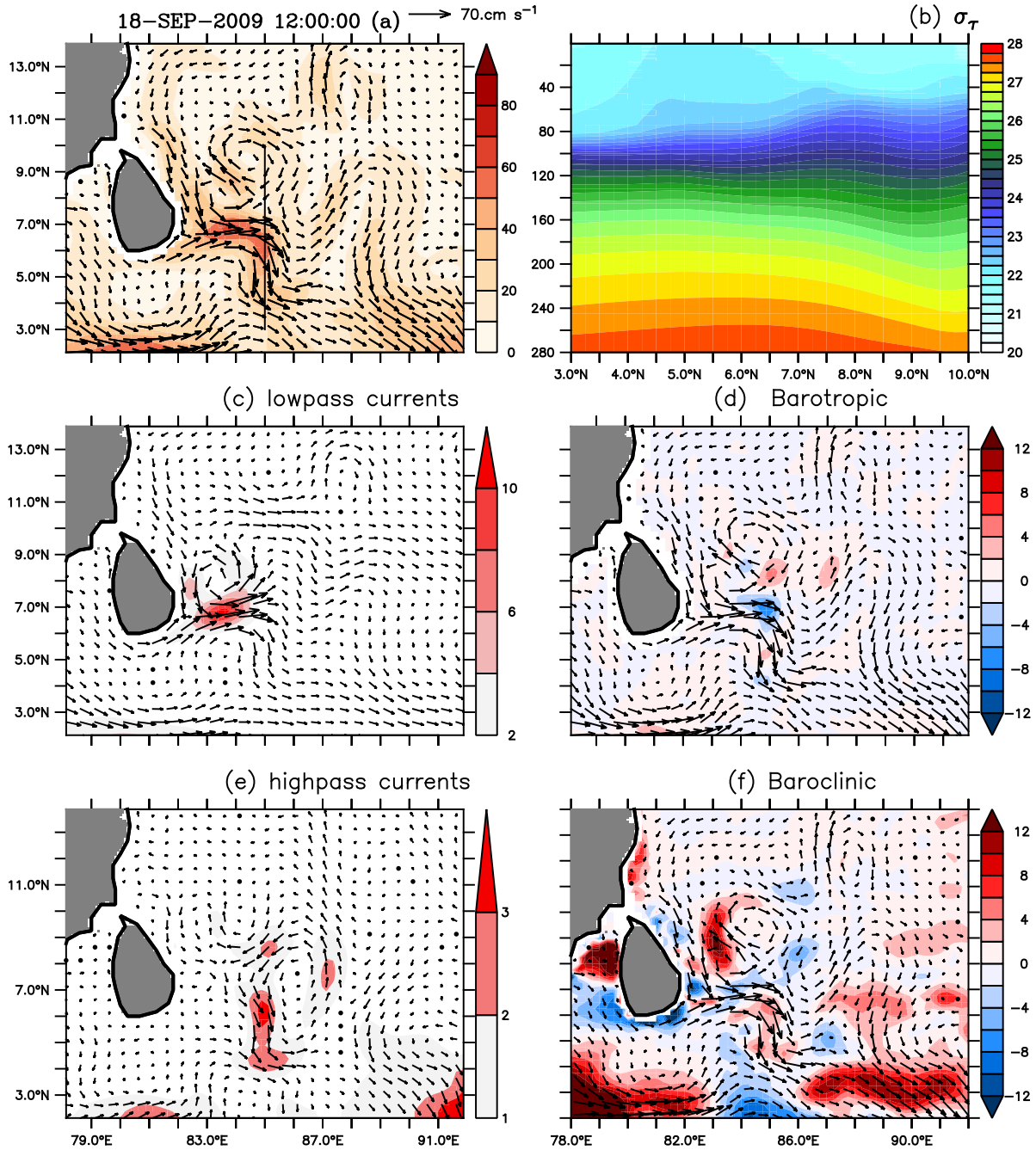


Figure 14: (a) Current vectors overlaid over speed (shading, cm/s) averaged over top 30m; (b)  $\sigma_t$  ( $\text{kg/m}^3$ ); (c) 120 day lowpass filtered currents (top 30m depth averaged) as mean flow overlaid over top 100 m vertically integrated map of MKE (shading,  $\text{cm}^3/\text{s}^2$ ); (d) Current vectors (top 30m depth averaged) overlaid over top 100 m vertically integrated map of barotropic energy conversion  $-u'_i u'_j \partial \bar{u}_i / \partial y$  (shading,  $\text{cm}^3/\text{s}^3$ ); (e) 120 day highpass filtered currents (cm/s) averaged over top 30 m, as eddies overlaid over top 100 m vertically integrated map of EKE (shading,  $10^6 \text{ cm}^3/\text{s}^2$ ); (f) Current vectors (top 30m depth averaged) overlaid over top 100 m vertically integrated map of baroclinic energy conversion (shading,  $\text{cm}^3/\text{s}^3$ ). All quantities are 5-day running averaged. Vectors are of same length in all panels and the scale vector is shown in above panel (a).

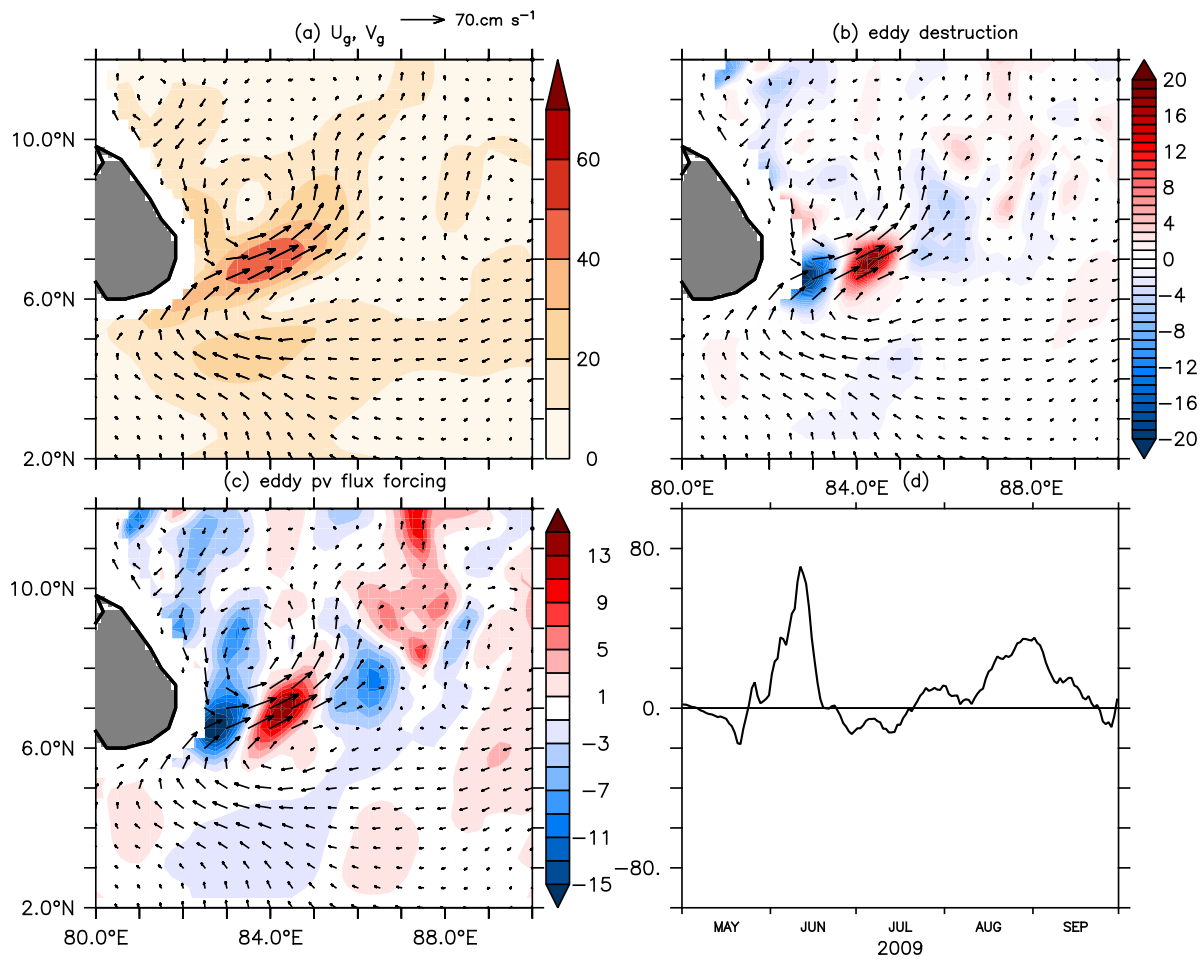


Figure 15: (Clockwise) At 50 m, time averaged (June-September) geostrophic currents vectors overlaid over speeds (shading,  $\text{cm/s}$ ); geostrophic current vectors overlaid over eddy enstrophy destruction term  $\mathbf{u}'q' \cdot \nabla \bar{q}$  (shading,  $10^{-16} \text{ cm/s}^2$ ); time series of eddy potential vorticity flux forcing,  $v'q'$  ( $10^{-5} \text{ cm/s}^2$ ) at  $84^\circ\text{E}$ ,  $6.5^\circ\text{N}$  and at 50 m depth; and eddy pv flux  $v'q'$  (shading,  $10^{-5} \text{ cm/s}^2$ ). Vectors are of the same scale as in Panel 1 (top left).

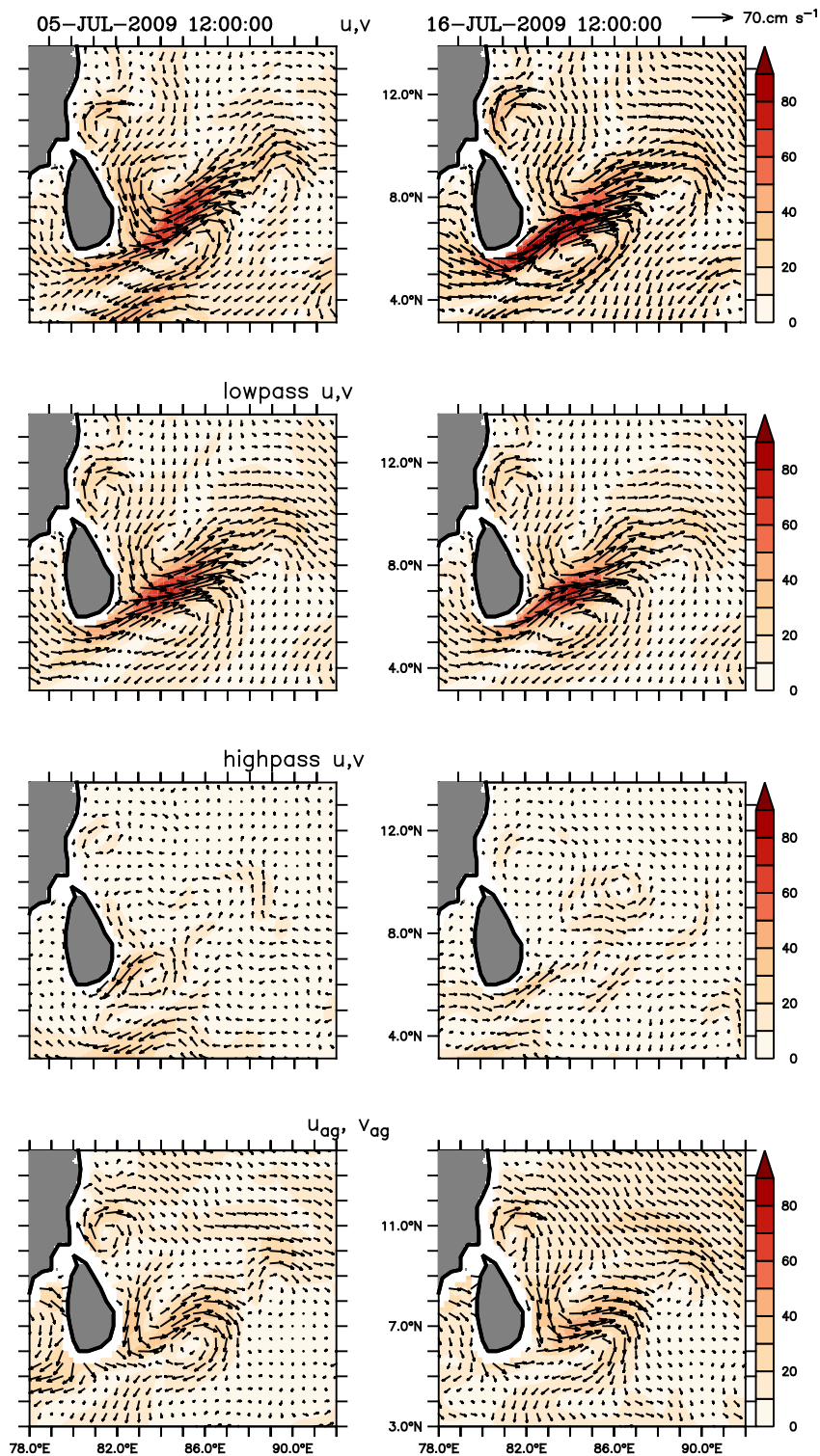


Figure 16: Snapshots of current vectors overlaid over speed (shading, cm/s) averaged over top 30m on 5/07/2009 (left panel) and 16/07/2009 (right panel). First row represents the model currents, second row represents the 120 day low-pass current components, third row shows the 120 day high-pass current components and the fourth row shows the ageostrophic current components. Vectors are of same length in all panels and the scale vector is shown in top panel.

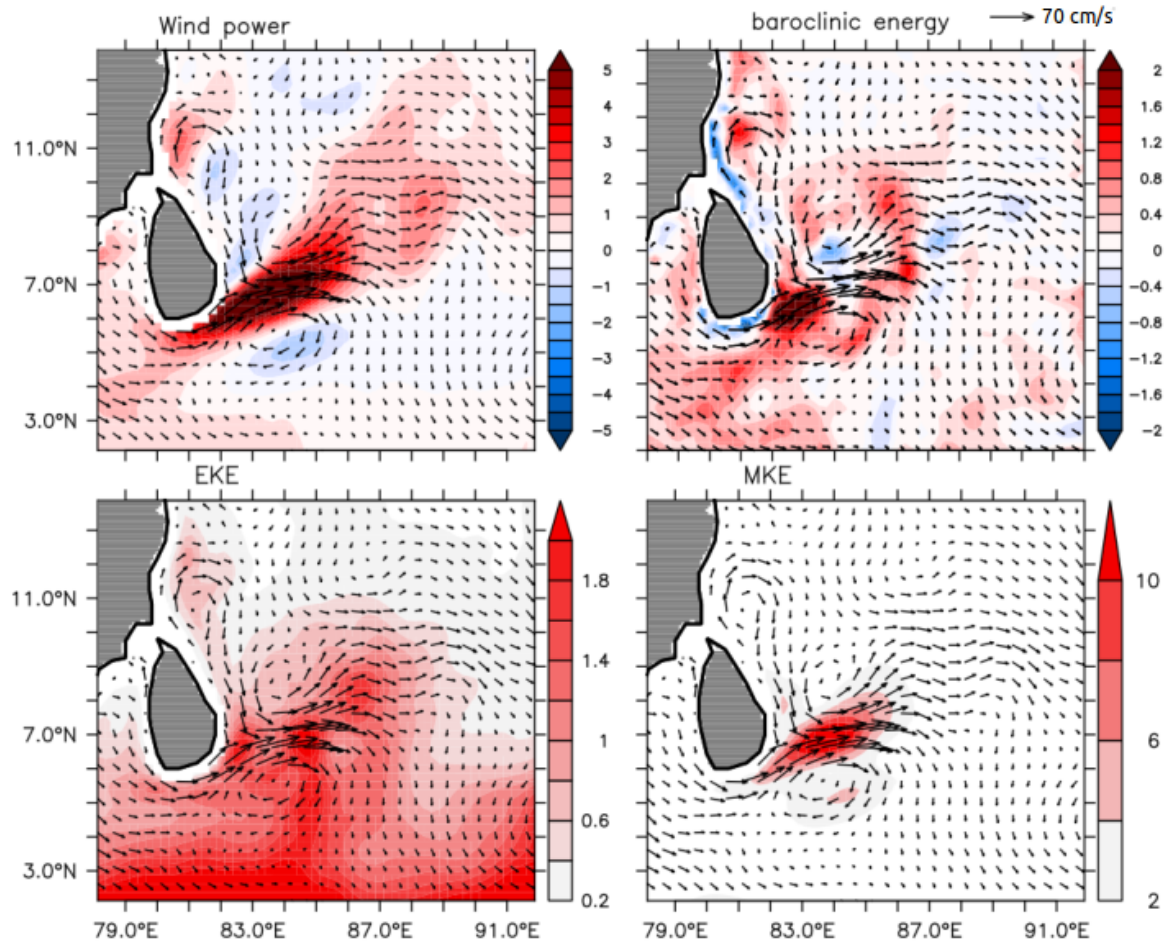


Figure 17: Clockwise: Time mean (June–September) maps of current vectors (averaged over top 30 m) overlaid over wind power (shading, watts); current vectors overlaid over vertically integrated (top 100 m) baroclinic energy conversions (shading,  $\text{cm}^3/\text{s}^3$ ); current vectors overlaid over vertically integrated (top 100 m) mean kinetic energy and eddy kinetic energy (shading,  $\text{cm}^3/\text{s}^2$ ).

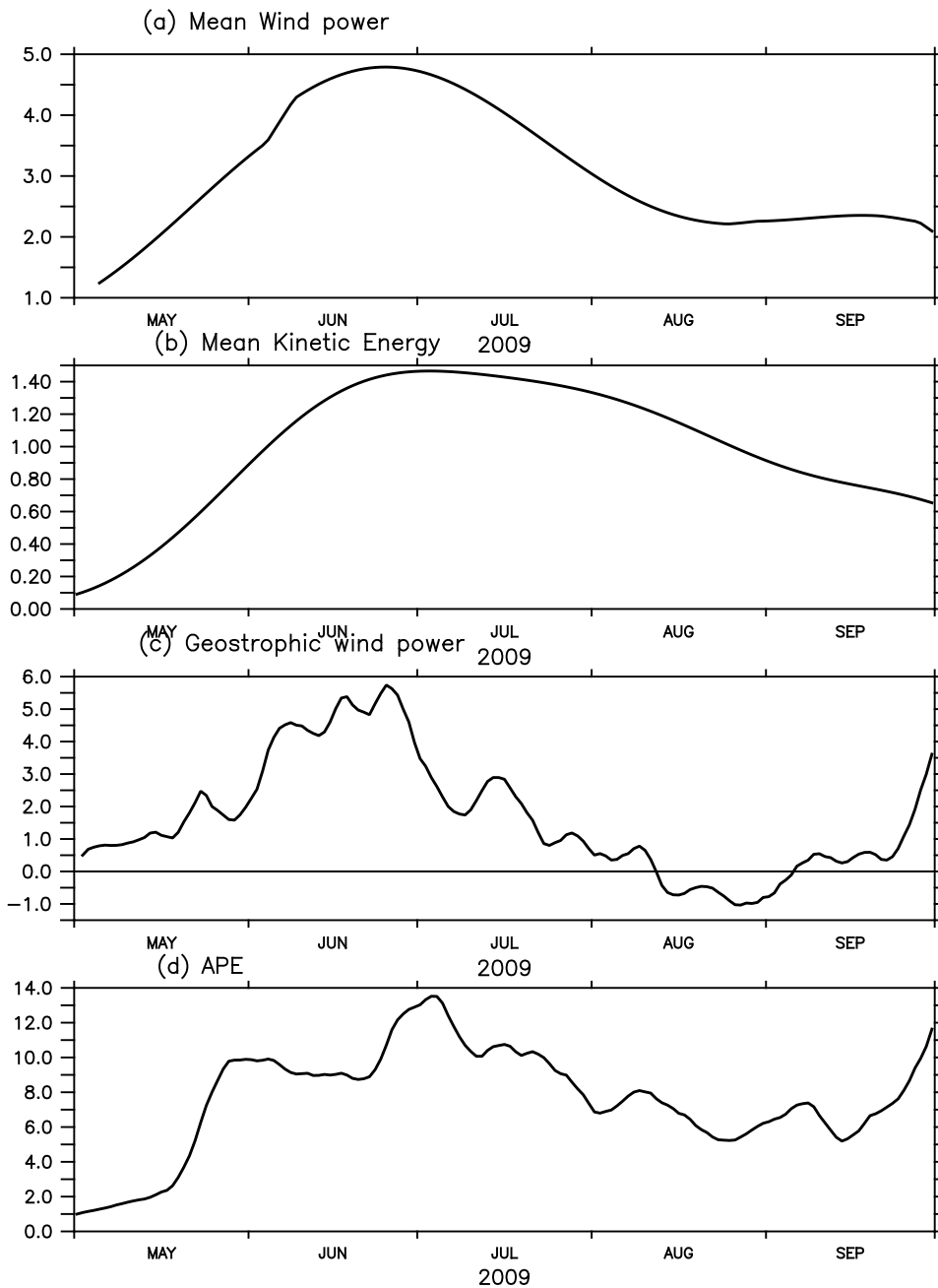


Figure 18: (a) Time series of area integrated ( $82\text{--}86^\circ\text{E}$ ,  $5\text{--}8^\circ\text{N}$ ) mean wind Power (5-day smoothed) (top) ( $10^9\text{ W}$ ) (b) surface integrated ( $82\text{--}86^\circ\text{E}$ ,  $5\text{--}8^\circ\text{N}$ ) MKE averaged over top 30 m (5-day smoothed) ( $10^{14}\text{ Joules/s}^2$ ); (c) Area integrated ( $82\text{--}86^\circ\text{E}$ ,  $5\text{--}8^\circ\text{N}$ ) geostrophic wind power (5-day smoothed) (top) ( $10^9\text{ W}$ ); (d) Volume integrated ( $82\text{--}86^\circ\text{E}$ ,  $5\text{--}8^\circ\text{N}$ , 0–100 m) APE (5-day smoothed) ( $10^{14}\text{ Joules}$ )